

MHD WAVES AND CORONAL HEATING: UNIFYING EMPIRICAL AND MHD TURBULENCE MODELS

Igor V. Sokolov¹, Bart van der Holst¹, Rona Oran¹, Cooper Downs², Ilia I. Roussev²,
Meng Jin¹, Ward B. Manchester IV¹, Rebekah M. Evans³, and Tamas I. Gombosi¹

Received _____; accepted _____

¹Department of AOSS, University of Michigan, 2455 Hayward St, Ann Arbor, MI 48109;
igorsok@umich.edu.

²Institute for Astronomy, University of Hawaii, 2680 Woodlawn Dr, Honolulu, HI 96822.

³Goddard Space Flight Center, Greenbelt, MD.

ABSTRACT

We present a new global model of the solar corona, including the low corona, the transition region and the top of chromosphere. The realistic 3D magnetic field is simulated using the data from the photospheric magnetic field measurements. The distinctive feature of the new model is incorporating the MHD Alfvén wave turbulence. We assume this turbulence and its non-linear dissipation to be the only momentum and energy source for heating the coronal plasma and driving the solar wind. The difference between the turbulence dissipation efficiency in coronal holes and that in closed field regions is because the non-linear cascade rate degrades in strongly anisotropic (imbalanced) turbulence in coronal holes (no inward propagating wave), thus resulting in colder coronal holes with the bi-modal solar wind originating from them. The detailed presentation of the theoretical model is illustrated with the synthetic images for multi-wavelength EUV emission compared with the observations from SDO AIA and Stereo EUVI instruments for the Carrington rotation 2107.

Subject headings: MHD—Alfvén waves—turbulence—coronal heating—heating function

1. Introduction

Results from Hinode observations have recently upped the estimates for the MHD wave energetics in the solar corona (*De Pontieu et al.* 2007). Observed in the chromosphere, the magnetic field perturbations appear to be so powerful that even a 10 ÷ 20% fraction of them, which propagate out from the Sun, carry a large enough energy to heat the solar corona and accelerate the solar wind. Even more promising, with the launch of the Solar Dynamics Observatory, we are now beginning to see observational hints of these ubiquitous

waves in the transition region and low corona (*McIntosh et al.* 2011).

Even before these encouraging observations had been obtained, models which incorporated, or even were entirely based upon Alfvén wave turbulence as the momentum and energy source were developed to describe the solar wind and coronal heating. Nowadays, *developing the turbulence-driven global space weather model* becomes a problem tempting to be solved.

1.1. Solar wind: can the turbulence-driven model compete with the semi-empirical one?

In *Usmanov et al.* (2000), a three-dimensional (3D) model for the solar wind was suggested in which the Alfvén wave turbulence pressure served to accelerate the solar wind. The solar wind bi-modal structure as observed by Ulysses was successfully reproduced in the numerical simulation. However, the quantitative agreement of this model with long history of the solar wind observations at 1 AU is insufficient for global space weather simulations. The same criticism seems to be applicable to the more refined and physics-based Alfvén-wave-driven models of the solar wind *Suzuki and Inutsuka* (2005); *Verdini et al.* (2010); *Osman et al.* (2011).

Therefore, the semi-empirical approach so far is better suited for global space weather simulations. The most popular parameterization was adopted by *Arge and Pizzo* (2000) in their Wang-Sheeley-Arge (WSA) model, which well describes the solar wind parameters at 1 AU. The semi-empirical “synoptic” formulae for the solar wind speed employ the solar magnetogram and the properties of the magnetic lines of the *potential magnetic field* as recovered from the synoptic magnetogram data. The empirical dependence of the solar wind properties from two input parameters: θ , which is the angular distance from the solar wind origin point till the nearest coronal hole boundary, and f_{exp} , which is the expansion factor, $f_{\text{exp}} = |\mathbf{B}_{R=R_{\odot}}| R_s^2 / [|\mathbf{B}_{R=2.5R_{\odot}}|(2.5R_s)^2]$, is derived from the following two

assumptions and observations. First, the slow solar wind is assumed to originate from the coronal hole boundary (small values of θ), whereas the fast solar wind originates from the central part of the coronal hole (large values of θ). Second, small coronal holes (having large values of f_{exp}) usually produce slower solar wind compared to large coronal holes (having small values of f_{exp}).

In *Cohen et al. (2007)*, we coupled the semi-empirical WSA formulae to the global three-dimensional model for the solar corona and inner heliosphere within the Space Weather Modeling Framework (SWMF) (*Tóth et al. 2005*). The WSA formulae were used as the boundary condition for the model which had been coupled to the MHD simulator via the varied polytropic index distribution (see *Roussev et al. (2003b)*). However, the physics of the Alfvén wave turbulence has almost no intersection with the semi-empirical model of WSA.

In order to be competitive with semi-empirical model of the solar wind, the turbulence-driven model should quantitatively reproduce the solar wind variation from the coronal hole boundary to the coronal hole central part, similar to that parameterized by the expansion factor.

1.2. Coronal heating: can the turbulence-based model compete with *ad hoc* heating functions?

Proceeding from the solar wind to the coronal heating, we can see again the disconnection between the physics-based models for the turbulent heating in the corona, one of the most advanced models of this kind being recently described in *Cranmer (2010)* (see also *Tu and Marsch (1997)*; *Hu et al. (2000)*; *Li and Habbal (2003)*; *Dmitruk et al. (2002)*) on one hand, and well established models with semi-empirical heating function, such as that presented in *Lionello et al. (2001)*; *Riley et al. (2006)*; *Titov et al. (2008)*; *Lionello et al. (2009)*; *Downs et al. (2010)*, on the other hand. The heating function is

applied to power the plasma in the solar corona with some heating rate, the distribution of which is given by some functions chosen not from some deep physical considerations, but chosen in an ad-hoc manner to provide a better agreement with observations.

These heating functions should be applied in conjunction with thermodynamic energy equation(s) in the Lower Corona (LC) model. A direct accounting is needed of the transition region between the chromosphere and the corona, where non-ideal-MHD thermodynamic terms of energy transport, such as electron heat conduction, radiative losses, and coronal heating all become important. In *Downs et al.* (2010) we used this thermodynamic MHD model to explore empirical parameterizations of coronal heating in the context of realistic 3D magnetic structures observed in the EUV and soft-X-Rays on Aug 27, 1996. Through direct comparison of synthetic observables to observations we demonstrated that this model can effectively capture the interplay between coronal heating and electron heat conduction.

The plasma parameters distribution obtained in this way may be successfully applied to generate synthetic EUV and X-ray images, which appear to be in a good agreement with those obtained with the EIT telescope onboard SOHO and SXT onboard Yohkoh (up to 2001). The observation synthesis capability has been extended to the major low corona imaging instruments available in space, namely STEREO/EUVI, SDO/AIA, and Hinode/XRT. The best agreement with observations is achieved with *ad hoc* heating functions (such as the unsigned-flux-based heating model as discussed in Section 2.1). *In order to be competitive with ad hoc coronal heating models, the turbulence-driven model should quantitatively reproduce some successful heating function, that is the realistic wave dissipation should provide the same heating rate, as, for example, the unsigned-flux-based heating model* Abbett (2007).

1.3. Towards a Global Alfvén-Wave-Turbulence-Driven MHD Model of the Solar Corona and Solar Wind

In addition to the mentioned disconnection between physics-based and observations-driven models, there are two more contradictions to comment on. First, the quantitative Alfvén-wave-driven models for the solar wind and for the coronal heating do not well conform with each other. For example, the coronal heating model of *Cranmer (2010)*, once applied to realistic 3D global model does not give realistic plasma parameters in the solar wind region (in the coronal holes). Second, the increased estimates for the Alfvén wave turbulence energetics in the Sun’s proximity require us to revisit the models for the evolution of turbulence while the solar wind propagates towards 1 AU. The revisited model should account for both *the observed level and frequency spectrum of turbulence at 1 AU and the solar wind ion temperature resulting from the turbulence dissipation.*

With the advent of modern computational tools it is now becoming the norm to employ detailed 3D computer models as simulation tools that directly account for the inhomogeneous nature of the Sun-Heliosphere environment. The key advantage of this approach is the ability to compare and validate model results through direct comparisons to all kinds of the observational data listed above: for the solar wind and turbulence characteristics at 1 AU (see also *Jin et al. (2012)*) and for EUV and X-ray images of the solar corona.

1.4. Goal and Content of the Paper

In the current paper, we get rid of the *ad hoc* heating functions and parameterize the coronal heating in the LC in terms of the Alfvén wave turbulence dissipation.

The theoretical model for this approach is summarized in Section 2. In subsections 2.1, 2.3 we demonstrate the possibility to parameterize a popular and successful semi-empirical

heating model based on unsigned magnetic flux in terms of the Alfvén wave turbulence dissipation. While choosing the way to parameterize heating, one may try to vary both the boundary condition for the wave energy flux (the Poynting flux) inflowing to the solar corona from the solar surface and the dissipation length for turbulence. In subsection 2.2 we show that the boundary condition is strongly restricted which reduces the model uncertainty. With the pre-specified boundary condition, the drastic difference in the plasma heating mechanism between open and closed field regions should be caused by a difference in the wave dissipation efficiency. In subsection 2.4 we suggest and describe the physical mechanism of a nonlinear interaction between *oppositely propagating waves*. The degraded intensity of the inward propagating waves may be responsible for the reduction in the turbulence dissipation rate in the coronal holes thus resulting in the bimodal solar wind structure.

In Section 3 we summarize a computational model and the code we use to simulate the state of the solar corona. Section 4 presents the simulation results for CR2107 and their comparison with EUV images. In the Conclusion we discuss the plans for a future.

2. Coronal Heating and Its Parameterization via the Alfvén Wave Turbulence

2.1. Coronal Heating Model Based on the Unsigned Magnetic Flux

Among the possible choices for the volumetric heating function examined in *Downs et al.* (2010), the most advantageous one reproduces both EUV and soft X-ray observations was that adopted earlier on by *Abbett* (2007). This heating function is based on the scaling law obtained by *Pevtsov et al.* (2003). This law establishes the power-law relationship between the total heating power, $E = \int e dV$, integrated over the plasma volume above $1 R_{\odot}$, and the unsigned magnetic flux, $\Phi = \int |\mathbf{B}_{R_{\odot}} \cdot \mathbf{dS}|$, integrated over the photospheric

surface, i.e.,

$$\int_{R \geq R_{\odot}} e dV = \text{const } \Phi, \quad \Phi = \int_{R=R_{\odot}} |\mathbf{B} \cdot d\mathbf{S}|. \quad (1)$$

Here R is the heliocentric distance and R_{\odot} is the solar radius. In the original work by *Pevtsov et al.* (2003), the relationship was found not to be linear: $E_X \approx 0.894\Phi^{1.1488}$ [CGSE]. Note, however, that the observational data used to derive the scaling law were the X-Ray total luminosity, E_X , which is only a small fraction of the total heating power, E . There are also losses due to the electron heat conduction, radiation in spectral ranges other than X-rays, and also solar wind expansion. As a result, a scaling factor that relates E_X to E is required, $\zeta = E_X/E \approx (1 \div 2) \cdot 10^{-2}$. If one assumes that E_X/E ratio is somewhat elevated during solar maximum, or near active regions where the average magnetic field strength, $|B|$, is higher, so that $\zeta \propto \Phi^{0.1488}$, then we can state that Eq.(1) is equivalent to that presented in *Abbett (2007); Pevtsov et al. (2003)*. On one hand, this relationship quantifies the well-known fact that during solar maximum, or near active regions, the average B is higher. On the other hand, the coronal heating is more intense in this case.

The constraint given by Eq.(1) is not sufficient to establish the 3D distribution of the heating function. In *Abbett (2007)*, the heating function was scaled with the magnetic field: $e \propto |\mathbf{B}|$, with the constant factor being chosen to satisfy a power-law scaling similar to Eq.(1). In *Downs et al. (2010)* an exponential envelope has been adopted: $e \propto |\mathbf{B}| \exp[-(R - R_{\odot})/L]$, where the dissipation length was chosen $L \approx 40$ Mm (herewith, R is the heliocentric distance). The latter formula, however, appears to be applicable only for closed field regions away from active regions. In coronal holes, in turn, the dissipation length was chosen to be by a factor of ten greater. In all the cases, the sophisticated envelope function had to be integrated over the volume in order to obtain the common constant factor satisfying Eq.(1).

Below we demonstrate that a model of coronal heating that both satisfies Eq.(1) and provides the spatial distribution of the heating envelope similar to that discussed above

can be realized assuming Alfvén waves being the main heating source the solar corona. Without going into details about the wave absorption and non-linear conversion and transport, we can construct the heating function by: (i) imposing a boundary condition for the Poynting flux of Alfvén wave energy; and, (ii) adopting an absorption mechanisms for the waves that would result in the desired distribution of energy deposition from waves into the coronal plasma.

2.2. “Percolation” Boundary Condition for the Poynting Flux at the Photosphere

Assuming that the Alfvén wave turbulence is the main source for heating the coronal plasma, here we discuss a choice of boundary condition for their Poynting vector, P at the solar surface. We consider that the local value of the Poynting flux at the photosphere, P_{R_\odot} , scales with the magnetic field magnitude, $|\mathbf{B}|_{R_\odot}$ as:

$$P_{R_\odot} = \text{const } |\mathbf{B}|_{R_\odot}. \quad (2)$$

With this choice for P , Eq.(1) is automatically satisfied if one assumes that the entire energy of the Alfvén waves traveling from the photosphere to the solar corona: $\int_{R=R_\odot} \frac{P_{R_\odot}}{|\mathbf{B}|_{R_\odot}} |\mathbf{B} \cdot d\mathbf{S}|$, is deposited into the coronal plasma, $\int_{R \geq R_\odot} e dV$. Then:

$$\begin{aligned} E &= \int_{R \geq R_\odot} e dV = \int_{R=R_\odot} \frac{P_{R_\odot}}{|\mathbf{B}|_{R_\odot}} |\mathbf{B} \cdot d\mathbf{S}| = \\ &= \frac{P_{R_\odot}}{|\mathbf{B}|_{R_\odot}} \int_{R=R_\odot} |\mathbf{B} \cdot d\mathbf{S}| = \frac{P_{R_\odot}}{|\mathbf{B}|_{R_\odot}} \Phi, \end{aligned}$$

meaning that Eq.(1) is fulfilled, and that the exact same constant is present in Eqs.(1,2):

$$\frac{E}{\Phi} = \frac{P_{R_\odot}}{|\mathbf{B}|_{R_\odot}}. \quad (3)$$

However, the relationship given by Eq.(1) is not the only way to arrive at Eq.(2). It can be also thought of as the *percolation* boundary condition for the Poynting flux of the

waves. Assume that all the magnetic field in the solar corona and all the Alfvén wave turbulence percolate to the solar corona from a depth at the solar interior where both the magnetic field intensity (presumably 50 – 70 kG) and the Alfvén wave Poynting flux are very high compared to their photospheric values (except in sunspots). In this case, both the magnetic field flux and the wave energy flux “propagate” along the flux tube, and they both vary inversely proportional to the flux tube cross-section. (Note that the growth of the flux tube cross-section from the solar interior towards the solar surface may be quite large and is hardly predictable.) As a consequence, the local value of the magnetic field at the photosphere is orders of magnitude smaller than that in the solar interior, and its variation along the solar surface may be quite large. The same behavior should be true for the Poynting flux. However, the *ratio* of the Poynting flux to the magnetic field intensity *remains constant along the magnetic tube*, and that is exactly what is assumed in Eq.(2).

Surprisingly, in addition to these two considerations, we can cite four different groups of authors, which arrive at the same condition as in Eq.(2) by quite different reasons (and stemming from quite different observations). First, the assumption as in Eq.(2) applied to the radial components of the Poynting flux, P_R , and the magnetic field, B_R , is a keystone of the Fisk theory for the solar wind (see *Fisk (1996)*; *Fisk et al. (1999b,a)*; *Fisk (2001)*; *Fisk and Schwadron (2001)*). Then, *Farrugia et al. (1997)* (and the works cited therein) formulated an “abnormal” adiabatic expansion law relating the (turbulent) energy density, w to the mass density, ρ : $w \propto \rho^{1/2}$ for the coronal matter, based on numerous observations relating to the coronal plasma and the CME ejecta. The suggested adiabatic law has an abnormal value of the adiabatic index: $w \propto \rho^\gamma$, $\gamma = \frac{1}{2} < 1$. Here, assuming a plasma dominated by turbulence, ρ is the mass density and w could be the energy density of the Alfvén waves ($w \sim (\delta B)^2$, with δB being the irregular magnetic field). As long as for the Alfvén waves $P = V_A w$, and the Alfvén wave speed scales with the density and magnetic field as $V_A = \frac{|\mathbf{B}|}{\sqrt{\mu_0 \rho}} \propto B \rho^{-1/2}$, Eq.(2) may be also rewritten in the form of the “abnormal”

adiabatic law,

$$w_{R_\odot} = \text{const} \sqrt{\mu_0 \rho} = \frac{P}{|\mathbf{B}|} \sqrt{\mu_0 \rho}. \quad (4)$$

As long as media with adiabatic index less than one are not thermodynamically stable, it is hardly instructive to interpret Eq.(2) in this manner. However, this unexpected support for Eq.(2) is worth mentioning here.

Another example supporting Eq.(2) is the paper by *Suzuki* (2006), which stems from the Wang-Sheeley-Argge model, and proposes a semi-empirical quantitative model for the solar wind. In their work, it is assumed that the solar wind is mostly powered by the Alfvén wave turbulence, and the input parameter in the model is the constant value of the following average: $\langle \delta \mathbf{B}_\perp \cdot \delta \mathbf{v}_\perp \rangle \approx 0.83 \text{ T m/s}$ at the solar surface. Here, $\delta \mathbf{B}_\perp$ and $\delta \mathbf{v}_\perp$ are the turbulent magnetic field and the turbulent velocity pulsation, respectively. These are both being orthogonal to the regular magnetic field. It is straightforward to demonstrate that the above assumption is equivalent to Eq.(2):

$$\langle \delta \mathbf{B}_\perp \cdot \delta \mathbf{v}_\perp \rangle = \frac{|\mathbf{B}| w}{V_A \rho} = \frac{|\mathbf{B}|^2 V_{Aw}}{\rho V_A^2 |\mathbf{B}|} = \mu_0 \frac{P_{R_\odot}}{|\mathbf{B}|_{R_\odot}}.$$

From here, one can see that the Alfvén wave turbulence may be employed to reproduce the observed solar wind parameters with the use of a boundary condition similar to that given by Eq.(2). In this case, the constraint for the constant factor in Eqs.(1,2) is $(P/|\mathbf{B}|)_{R_\odot} \geq (0.83 \text{ T m/s})/\mu_0 \approx 7 \cdot 10^5 \text{ W}/(\text{m}^2\text{T})$. This is the lower bound as long as in the model of *Suzuki* (2006) there is no energy loss mechanism from the solar wind plasma (e.g. radiation, heat conduction, etc.). Therefore, the realistic heating rate should be higher in order to balance these losses. Nevertheless, the estimate is very close to that which follows from *Pevtsov et al.* (2003); *Abbett* (2007); *Downs et al.* (2010). Specifically, for the choice $\zeta = 2 \cdot 10^{-2} \langle |\mathbf{B}|[\text{G}] \rangle^{0.1488}$, where the average magnetic field intensity over the solar surface is introduced, the estimate of the Pointing-flux-to-field ratio is as follows:

$$\frac{E}{\Phi} = \frac{E_X}{\Phi \zeta} \left(\approx \frac{0.894 \Phi^{1.1488}}{2 \cdot 10^{-2} |\mathbf{B}|^{0.1488} \Phi} \approx 44.7 (4\pi R_\odot^2)^{0.1488} [\text{CGSE}] \right) \approx 1.1 \cdot 10^6 \frac{\text{W}}{\text{m}^2\text{T}},$$

or, in all equivalent forms:

$$\begin{aligned}
 P &\approx 1.1 \cdot 10^6 \frac{\text{W}}{\text{m}^2} \left[\frac{|B|}{1 \text{ T}} \right], & P_R &\approx 1.1 \cdot 10^6 \frac{\text{W}}{\text{m}^2} \left[\frac{|B_R|}{1 \text{ T}} \right], \\
 w = \frac{P}{V_A} &\approx 6.6 \cdot 10^{-3} \text{W/m}^3 \sqrt{\frac{\rho}{3 \cdot 10^{-11} \text{kg/m}^3}}, & \langle \delta \mathbf{B}_\perp \cdot \delta \mathbf{v}_\perp \rangle &\approx 1.4 \text{Tm/s} \\
 \langle \delta \mathbf{v}_\perp \cdot \delta \mathbf{v}_\perp \rangle &\approx (15 \text{ km/s})^2 \sqrt{\frac{3 \cdot 10^{-11} \text{kg/m}^3}{\rho}},
 \end{aligned} \tag{5}$$

where we chose the value of mass density $3 \cdot 10^{-11} \text{kg/m}^3$ ($N_a \approx 2 \cdot 10^{16} \text{m}^{-3}$) corresponding to the top of the chromosphere (near the transition region), to compare with the Hinode observations of the turbulent velocities $\approx 15 \text{ km/s}$. Thus, a variety of models, which are validated against EUV observations, X-ray radiance measurements, as well as in-situ solar wind observations are *all in agreement* with Eq.(2), with a rather narrow range for the constant factor in the expression.

Next, let us compare this boundary condition with a coronal heating model based on Alfvén wave turbulence, such as the advanced model of *Cranmer* (2010) (see also the works cited therein). By comparing Eq.(2) with Eq.(29) from *Cranmer* (2010), one can see that Eq.(2) is adopted in their model not just as a boundary condition at the solar surface, but as a fundamental relationship valid throughout the solar corona (or, at least, for heliocentric distances $1.1R_\odot \leq R \leq 1.5R_\odot$). The observational constraints for the constant factor in Eq.(2) are somewhat weaker than the values discussed here ($P/|\mathbf{B}| \sim (0.5 \div 0.8 \div 1.0) \cdot 10^6 \text{W}/(\text{m}^2\text{T})$). However, the deviation is very small. In addition, there is some uncertainty in these observations (e.g., the Pointing flux is not measured, but rather the oscillating velocity). Also, the solar observations at $1.1R_\odot$ cannot be easily converted into a boundary condition at the photosphere. Furthermore, the dissipation length of 40 Mm assumed by *Downs et al.* (2010) is shorter than the difference between $1.1 R_\odot$ (where the oscillations are observed) and $1 R_\odot$ (where the boundary condition is imposed). As a consequence, it is likely that the turbulence observed at $1.1 R_\odot$ is already weakened by the wave absorption.

2.3. Heating Function Parameterized in Terms of Alfvén Wave Dissipation

In order to proceed to the 3D distribution of the heating function, we represent the volume integral of the heating function as the total of integrals over the flux tubes:

$$E = \int \left(\int e dS(\ell) \right) d\ell,$$

with $d\ell$ being the length differential along the flux tube, and $dS(\ell)$ being the expanding cross-section of the flux tube. Along the flux tube, the magnetic flux is conserved, and hence: $dS(\ell)|\mathbf{B}|(\ell) = \text{const} = |(\mathbf{B} \cdot d\mathbf{S})|$. Again, assuming that the Alfvén waves propagate only along the flux tube, their energy conservation is given by the following relationship: $P(\ell + d\ell)dS(\ell + d\ell) - P(\ell)dS(\ell) = -e d\ell dS(\ell)$, hence:

$$\frac{e(\ell)}{|\mathbf{B}|(\ell)} = -\frac{\partial}{\partial \ell} \left(\frac{P(\ell)}{|\mathbf{B}|(\ell)} \right). \quad (6)$$

By introducing the absorption length, L , such that $e = V_A w/L = P/L$, one can integrate Eq.(6) along the magnetic field line:

$$\begin{aligned} P(\ell) &= \left(\frac{P}{|\mathbf{B}|} \right)_{R=R_\odot} |\mathbf{B}|(\ell) \exp \left(- \int_0^\ell \frac{d\ell}{L} \right), \\ e(\ell) &= \left(\frac{P}{|\mathbf{B}|} \right)_{R=R_\odot} \frac{|\mathbf{B}|(\ell)}{L} \exp \left(- \int_0^\ell \frac{d\ell}{L} \right). \end{aligned} \quad (7)$$

Depending on the choice of the absorption length, one can obtain the following spatial distribution of the heating function: (i) $l \ll L$, the heating function is the same as that as used in *Abbett (2007)*, i.e., $e \propto |\mathbf{B}|$; (ii) for $l \gg L$, the heating function decays exponentially, i.e., $e \propto \exp(-\int d\ell/L)$. We now arrive at an important conclusion, that is, *the most common heating functions may be parameterized in terms of an effective absorption coefficients for the Alfvén wave turbulence!* The desired absorption coefficient, V_A/L , may be directly included to the WKB equation for total wave intensities, w_\pm , propagating parallel and antiparallel to the mean magnetic field vector, $\mathbf{b} = \mathbf{B}/|\mathbf{B}|$, correspondingly (*Usmanov et al. 2000*):

$$\frac{\partial w_\pm}{\partial t} + \nabla \cdot (\mathbf{u} w_\pm \pm \mathbf{b} V_A w_\pm) + \frac{1}{2} w_\pm (\nabla \cdot \mathbf{u}) = -\frac{V_A w_\pm}{L}. \quad (8)$$

In the open field region (in the solar wind) only outward propagation waves were involved in the (*Usmanov et al.* 2000) heliosphere model, that is the “plus” waves in the regions of the solar wind with the positive radial magnetic field and the “minus” waves elsewhere. In addition to this, the low solar corona model of the present paper also includes the closed field regions, where the waves of both directions are present emitted from the opposite footpoints of a closed magnetic field line. However, Eq.(8) can only be applied as a rather crude approximation. In the more refined model as derived in *Sokolov et al.* (2009)) on the left hand side of Eq.(8) the term proportional to the velocity divergence and spectral evolution in the convergent/divergent flows should be properly accounted for. Even more important is the role played by the frequency dependence on the right hand side of Eq.(8):

$$\frac{\partial I_{\pm}}{\partial t} + \nabla \cdot (\mathbf{u}I_{\pm} \pm \mathbf{b}V_A I_{\pm}) - \frac{\omega}{2} \frac{\partial I_{\pm}}{\partial \omega} (\nabla \cdot \mathbf{u}) = -\Gamma(\omega)I_{\pm}, \quad (9)$$

where the equations are formulated for the wave energy density, I_{\pm} , related to the unit volume and to the interval of the wave circular frequency, $d\omega$, in the co-moving frame of reference, so that $w_{\pm} = \int_0^{\infty} I_{\pm} d\omega$. Not only is the dependence of the dissipation coefficient, $\Gamma(\omega)$, on the wave frequency significant (practically so that only for the highest wave frequencies is the absorption non-negligible), but also the nonlinear wave-wave interaction may occur in the form of the wave package upshift in frequency. As a result, the wave energy from large-scale perturbations flows through the spectrum towards the short-scale end and once transferred to the shortest possible scales, the energy dissipates.

2.3.1. Kolmogorov Turbulence and Dissipation

We found above that the unsigned-flux-based heating function with the exponential envelope function can be realized as the dissipation in the Alfvén wave turbulence. In (*Downs et al.* 2010) we saw that the unsigned-flux-based heating function well reproduces EUV and X-ray images of the closed field regions (about the coronal holes, see below) with the choice for the dissipation length to be ≈ 40 Mm. Here we discuss a choice for the

dissipation length, L , based on the phenomenological turbulence theory, desiring that in the closed field region L would be about 40 Mm and do not vary too strongly, at least at low altitudes $\leq 0.1R_\odot \approx 70$ Mm.

Consider extra terms in the governing equations for the Alfvén, turbulent energy density, accounting for the wave-wave ‘cascade’ rate. Only the cascade-describing terms are kept. For the closed field region we employ the key assumption about the *isotropic (balanced)* turbulence:

$$I_+ = I_- = I. \quad (10)$$

For simplicity, assume that $\Gamma_{ww}(\omega)$ characterizes the rate of conversion of two wave “photons” of the frequency of $\sim \omega$ to a single photon with the frequency, $\sim 2\omega$. As long as the wave energy conserves in this processes, this may be thought of as the conservative advection in the frequency space. The positive speed of this advection being approximately $\sim \omega\Gamma_{ww}(\omega)$, as long as with the rate, Γ_{ww} the wave frequency is upshifted by $[(\sim 2\omega) - (\sim \omega)]$. So, we have a phenomenological equation as follows:

$$\frac{\partial I}{\partial t} + \frac{\partial}{\partial \omega} (\omega\Gamma_{ww}(\omega)I) = -\Gamma(\omega)I \quad (11)$$

The dimensionless ratio, Γ_{ww}/ω , may be parameterized in terms of another dimensionless ratio, $\omega I\mu_0/B^2$, B being the magnetic field magnitude. For two most natural estimates, $\Gamma_{ww} \propto \omega \cdot (\omega I\mu_0/B^2) \propto \omega(\delta B/B)^2$ or $\Gamma_{ww} \propto \omega\sqrt{\omega I\mu_0/B^2} \propto \omega(\delta B/B)$, we arrive at the Kraichnan spectrum or the Kolmogorov spectrum (see *Li et al. (2011)*) as the steady-state solution of Eq.(11) throughout the inertial range of frequencies (we neglect wave absorption in this range):

$$\frac{\partial}{\partial \omega} \left[\omega^2 \left(\frac{\omega I\mu_0}{B^2} \right)^{0.5;1} I \right] = 0$$

for $I \propto \omega^{-\frac{5}{3};-\frac{3}{2}}$. We chose the assumption of the Kolmogorov spectrum, so that

$$\Gamma_{ww} \propto \frac{\omega}{V_A} \sqrt{\frac{\omega I}{\rho}}.$$

On integrating Eq.(11) over frequency from some frequency value within the inertial range, ω_{in} , to infinity with neglecting wave dissipation within the inertial range, we find:

$$\int_{\omega_{in}}^{\infty} \Gamma(\omega) I d\omega \propto \left(\frac{\omega^2 I}{V_A} \sqrt{\frac{\omega I}{\rho}} \right)_{\omega=\omega_{in}}. \quad (12)$$

The equation is valid for any choice of ω_{in} within the inertial range, as long as the right hand side is constant for $I \propto \omega^{-5/3}$ and $\Gamma(\omega_{in}) = 0$. The energy of the Kolmogorov spectrum, $\propto \int \omega^{-5/3} d\omega$, is concentrated at low frequency, therefore, at the least possible $\omega_{in} \sim \omega_{min}$ one can estimate $(\omega I)_{\omega=\omega_{min}} \sim w$ and

$$\int_{\omega_{in}}^{\infty} \Gamma(\omega) I d\omega \propto \frac{\omega_{min}}{V_A} \sqrt{\frac{w}{\rho}} w,$$

Following *Hollweg* (1986), for an isotropic Alfvén wave turbulence we accept

$$\int_{\omega_{in}}^{\infty} \Gamma(\omega) I d\omega \approx \frac{1}{L_{\perp}} \sqrt{\frac{w}{\rho}} w = \frac{\sqrt{\langle \delta \mathbf{v}_{\perp} \cdot \delta \mathbf{v}_{\perp} \rangle}}{L_{\perp}} w, \quad (13)$$

so that the total volumetric heating rate due to the turbulent energy dissipation equals:

$$e = \frac{1}{L_{\perp}} \sqrt{\frac{w = w_{-} = w_{+}}{\rho}} (w_{-} + w_{+}). \quad (14)$$

The introduction of $L_{\perp} \propto 1/k_{\perp}$, which is *the transverse correlation length of turbulence* instead of $\omega/V_A = k_{\parallel}$, which is the wave vector for the Alfvén wave propagating *along* the magnetic field line, makes the cascade theory better suited to the nature of purely transverse Alfvén waves. For such waves, the ratio of the *transverse* turbulent velocity to the *longitudinal* wavelength could hardly characterize the rate of nonlinear wave dissipation. In more refined turbulent theory (which we do not apply and even do not review here) the spectral energy should be introduced separately for parallel and transverse wave vectors. However, within our *phenomenological approach we assume that $k_{\perp} \propto k_{\parallel}$* and combine, once needed, the spectral energy distribution over $\omega = V_A k_{\parallel}$ with the transverse correlation length, to quantify the non-linear dissipation rate.

To close the model and to compare its predictions with the unsigned-flux-based heating function, we chose, again following *Hollweg* (1986), the scaling law for the transverse

correlation length:

$$L_{\perp} \propto |\mathbf{B}|^{-1/2}, \quad L_{\perp} = \frac{75 [\text{km} \cdot \text{T}^{1/2}]}{\sqrt{|\mathbf{B}|}}. \quad (15)$$

In the present work we use the following range of values for the empirical constant:

$L_{\perp} \sqrt{|\mathbf{B}|}$:

$$50 [\text{km} \cdot \text{T}^{1/2}] \leq L_{\perp} \sqrt{|\mathbf{B}|} \leq 100 [\text{km} \cdot \text{T}^{1/2}]$$

in the numerical estimates below we use $L_{\perp} \sqrt{|\mathbf{B}|} \approx 75 [\text{km} \cdot \text{T}^{1/2}]$ from *Hollweg* (1986).

The scaling law $|\mathbf{B}|L_{\perp}^2 = \text{const}$ is well compatible with the “percolation hypothesis” noticed above: while waves propagating from the solar interior along the flux tube towards the solar surface it is natural to assume that L_{\perp}^2 varies proportionally to the flux tube cross-section

To discuss the value and the variability of the spatial scale in the coronal heating, if the latter is related to the Alfvén wave turbulence dissipation, compare Eqs.(14,15) with the representation of the wave dissipation as in the right hand side of Eq.(8). From this comparison we find: $V_A/L = \sqrt{w/\rho}/L_{\perp}$. At the corona base we can employ Eq.(4) to evaluate the boundary values of w and the estimate for L in this region reads:

$$L = \frac{V_A(L_{\perp} \sqrt{|\mathbf{B}|})}{\sqrt{\frac{|\mathbf{B}|(\frac{P}{|\mathbf{B}|})\sqrt{\mu_0\rho}}{\rho}}} \approx \sqrt{\frac{V_A}{400 \text{ km/s}}} 40 \text{ Mm}.$$

We see that with the choice of the above estimates for the transverse correlation length and for the boundary condition for the Poynting flux the estimate of the dissipation length at the coronal base has only weak scaling (as a square root) with the Alfvén speed. The latter does not vary too much at the coronal base, as long as $V_A \propto |\mathbf{B}|/\sqrt{\rho}$ and the density correlates with the magnetic field intensity, being larger in the active regions with strong magnetic fields. We also see that for a reasonable estimate for the Alfvén speed at the coronal base, $V_A \sim (200 - 500) \text{ km/s}$, the dissipation length is close to the *ad hoc* value $L = 40 \text{ Mm}$ as used in *Downs et al.* (2010). The dissipation length is not used below directly, as long as Eqs.(14,15) do not include it. However, the capability to reproduce the

popular unsigned-flux-based heating model with the popular envelop function is important. We can now strengthen the conclusion above in the following manner: *the choice of a boundary condition for the Poynting flux together with the estimates of the non-linear dissipation in an isotropic Kolmogorov turbulence allows us to reproduce in detail the unsigned-flux-based ad hoc heating model for the closed field region.*

2.4. Coronal Holes and the Solar Wind Model

An important *ad hoc* approach while applying the heating function is the capability to use strongly different functions in the coronal holes and in the closed field regions. In *Downs et al. (2010)*; *Lionello et al. (2009)* in the coronal holes the following heating function was applied:

$$e = 5 \cdot 10^{-7} \exp[-(R - R_{\odot})/(0.7R_{\odot})] \text{ erg/cm}^3\text{s}.$$

Comparing with the unsigned-flux-based model for the closed field region, the spatial scale of the heating function in the coronal holes is significantly longer than ~ 40 Mm which we used above.

Here, we discuss the possibility of implementing such a heating model via the Alfvén wave absorption. First, we do not assume that in the coronal holes the Poynting flux at the corona base is different from that in the closed field region and attribute the drastic difference in the heating functions to the difference in the dissipation rate only. Second, comparing the integral of the heating function over the coronal hole volume with the accepted value of the Poynting flux for the turbulence, one can find that only a few percents of the Poynting flux is absorbed in the coronal holes within the heliocentric distance range. $R_{\odot} \leq R \leq 2.5R_{\odot}$.

Comparing with the closed field region, where almost all wave energy is absorbed, one can conclude that the wave energy dissipation rate in coronal holes should include a small

factor of the order of a few percents compared with Eqs.(14,15).

2.4.1. Imbalanced Kolmogorov Turbulence and its Dissipation

The drastic decrease in the wave dissipation rate in the coronal holes comes naturally if we take into account a strong turbulence anisotropy in the coronal holes: the outward propagating waves should be much more intense than the waves propagating toward the Sun. Below, having in mind that the *anisotropy* is a natural property of any MHD turbulence in the directional magnetic field, the turbulence in the coronal holes is referred to as *imbalanced*, not anisotropic.

Now we consider an imbalanced turbulence, such that $I_+ \neq I_-$. As long as the real cascade physics requires the presence of oppositely propagating waves, we require that the *wave-wave interaction rate should be the function of minimum of w_-, w_+ in a strongly imbalanced turbulence*. To achieve this, instead of Eq.(14) we use the following expression for the dissipation rate:

$$e = \frac{\sqrt{|\mathbf{B}|}}{(L_\perp \sqrt{|\mathbf{B}|})} \left(\sqrt{\frac{w_+}{\rho}} w_- + \sqrt{\frac{w_-}{\rho}} w_+ \right). \quad (16)$$

For the closed field region this expression is more realistic than that we used before, as long it correctly captures more intense heating in shorter loops, in which the intensities of the oppositely propagating waves are more uniform, as compared to longer loops, in which the wave energy for counter-propagating waves may be strongly non-uniform and imbalanced. However, for coronal holes this approximation is not sufficient as long as the WKB approximation, under which Eq.(11) was derived is not accurate enough. Within the model we use here, in the coronal holes only outward propagating waves can exist. while in reality the wave outward propagation is accompanied with some reflection, resulting in appearance of waves propagating towards the Sun. Small ratio of the reflected wave amplitude to the bulk wave amplitude is described by the reflection coefficient, C_{refl} .

Therefore, the negligibly small $\min(w_{\pm})$ in the expression for the dissipation rate should be floored with $C_{\text{refl}}^2 \max(w_{\pm})$, giving an ultimate expression for the turbulent dissipation rate we use in the present work:

$$e = \frac{\sqrt{|\mathbf{B}|}}{(L_{\perp} \sqrt{|\mathbf{B}|})} \left(\sqrt{\frac{\max(w_+, C_{\text{refl}}^2 w_-)}{\rho}} w_- + \sqrt{\frac{\max(w_-, C_{\text{refl}}^2 w_+)}{\rho}} w_+ \right). \quad (17)$$

2.4.2. How to Derive Eq.(16)?

In order to justify the Eqs.(16,17), we outline the way to derive them consistently. One can employ the framework of reduced MHD, which solves the equations of motion, induction and continuity:

$$\begin{aligned} \frac{\partial \mathbf{u}}{\partial t} + (\mathbf{u} \cdot \nabla) \mathbf{u} + \frac{\nabla B^2}{\mu_u \rho} + \frac{\nabla(P_e + P_i)}{\rho} &= \frac{(\mathbf{B} \cdot \nabla) \mathbf{B}}{\mu_0 \rho}, \\ \frac{\partial \mathbf{B}}{\partial t} + (\mathbf{u} \cdot \nabla) \mathbf{B} + \mathbf{B}(\nabla \cdot \mathbf{u}) &= (\mathbf{B} \cdot \nabla) \mathbf{u}, \\ \frac{\partial \rho}{\partial t} + \nabla \cdot (\rho \mathbf{u}) &= 0, \end{aligned}$$

by means of representing the magnetic field and velocity vectors as sums of regular and turbulent parts, $\mathbf{u} = \tilde{\mathbf{u}} + \delta \mathbf{u}$, $\mathbf{B} = \tilde{\mathbf{B}} + \delta \mathbf{B}$ (below tildes are omitted) and by simplifying the equations for turbulent amplitudes:

$$\frac{\partial \delta \mathbf{u}}{\partial t} + (\mathbf{u} \cdot \nabla) \delta \mathbf{u} + (\delta \mathbf{u} \cdot \nabla) \delta \mathbf{u} + (\delta \mathbf{u} \cdot \nabla) \mathbf{u} = \frac{(\mathbf{B} \cdot \nabla) \delta \mathbf{B}}{\mu_0 \rho} + \frac{(\delta \mathbf{B} \cdot \nabla) \delta \mathbf{B}}{\mu_0 \rho} + \frac{(\delta \mathbf{B} \cdot \nabla) \mathbf{B}}{\mu_0 \rho}, \quad (18)$$

$$\frac{\partial \delta \mathbf{B}}{\partial t} + (\mathbf{u} \cdot \nabla) \delta \mathbf{B} + (\delta \mathbf{u} \cdot \nabla) \delta \mathbf{B} + (\delta \mathbf{u} \cdot \nabla) \mathbf{B} + \delta \mathbf{B}(\nabla \cdot \mathbf{u}) = (\mathbf{B} \cdot \nabla) \delta \mathbf{u} + (\delta \mathbf{B} \cdot \nabla) \delta \mathbf{u} + (\delta \mathbf{B} \cdot \nabla) \mathbf{u}, \quad (19)$$

$$\frac{\partial \rho}{\partial t} + (\mathbf{u} \cdot \nabla) \rho + (\delta \mathbf{u} \cdot \nabla) \rho + \rho \nabla \cdot \mathbf{u} = 0, \quad (20)$$

by assuming the incompressibility conditions: $\nabla \cdot \delta \mathbf{u} = 0$, $\mathbf{B} \cdot \delta \mathbf{B} = 0$. The equations for the Elsasser variables, $\mathbf{z}_{\pm} = \delta \mathbf{u} \mp \delta \mathbf{B} / \sqrt{\mu_0 \rho}$ are obtained as the sum Eq.(18) $\mp \frac{1}{\sqrt{\mu_0 \rho}} \times$ Eq.(19) $\pm \frac{\delta \mathbf{B}}{\rho \sqrt{\mu_0 \rho}} \times$ Eq.(20):

$$\frac{d_{\pm} \mathbf{z}_{\pm}}{dt} + \mathbf{z}_{\mp} \cdot \nabla \mathbf{u} \mp \frac{\mathbf{z}_{\mp} \cdot \nabla \mathbf{B}}{\sqrt{\mu_0 \rho}} - \frac{\mathbf{z}_{\pm} - \mathbf{z}_{\mp}}{4\rho} \frac{d_{\mp} \rho}{dt} = 0,$$

where $\frac{d_{\pm}}{dt} = \frac{\partial}{\partial t} + (\mathbf{u} \pm \mathbf{V}_A + \mathbf{z}_{\mp}) \cdot \nabla$ and $\mathbf{V}_A = \frac{\mathbf{B}}{\sqrt{\mu_0 \rho}}$. The dynamic equations for the wave energy densities, $w_{\pm} = \rho \mathbf{z}_{\pm}^2 / 4$, may be obtained by multiplying the above equation by $\rho \mathbf{z}_{\pm} / 2$ and adding Eq.(20) $\times 3 \mathbf{z}_{\pm}^2 / 8$:

$$\frac{\partial w_{\pm}}{\partial t} + \nabla \cdot [(\mathbf{u} \pm \mathbf{V}_A + \mathbf{z}_{\mp}) w_{\pm}] + \frac{w_{\pm}}{2} (\nabla \cdot \mathbf{u}) + \frac{\rho}{2} \mathbf{z}_{\pm} \cdot [(\mathbf{z}_{\mp} \cdot \nabla) \mathbf{u} \mp \frac{(\mathbf{z}_{\mp} \cdot \nabla) \mathbf{B}}{\sqrt{\mu_0 \rho}}] + \frac{\mathbf{z}_{+} \cdot \mathbf{z}_{-}}{8} \frac{d_{\mp} \rho}{dt} = 0.$$

As the first (WKB) approximation one can set $\mathbf{z}_{\mp} = 0$ in the equations for w_{\pm} and obtain:

$$\frac{\partial w_{\pm}}{\partial t} + \nabla \cdot [(\mathbf{u} \pm \mathbf{V}_A) w_{\pm}] + \frac{w_{\pm}}{2} (\nabla \cdot \mathbf{u}) = 0.$$

This equation describes Alfvén wave propagation along the magnetic field lines (first two terms) and the wave energy reduction in the expanding plasma (the last term) because of the work done by the wave pressure $P_w = \frac{1}{2}(w_{+} + w_{-})$. Within the more accurate approximation the non-linear term $\nabla \cdot (\mathbf{z}_{\mp} w_{\pm})$ results in the turbulent cascade and the wave energy dissipation. The dissipation rate for the wave energy density, w_{+} , is controlled by the amplitude of the oppositely propagating wave, $|\mathbf{z}_{-}| \sim \sqrt{w_{-}/\rho}$, and the correlation length, L_{\perp} , in the transverse (with respect to the magnetic field) direction, because in the Alfvén wave, propagating along the magnetic field, $\delta \mathbf{u}$, $\delta \mathbf{B}$ are perpendicular to the magnetic field. Therefore, $\nabla \cdot (\mathbf{z}_{\mp} w_{\pm}) \sim \frac{1}{L_{\perp}} \sqrt{\frac{w_{\mp}}{\rho}} w_{\pm}$ and the WKB equations with an account for non-linear dissipation read:

$$\begin{aligned} \frac{\partial w_{+}}{\partial t} + \nabla \cdot [(\mathbf{u} + \mathbf{V}_A) w_{+}] + \frac{w_{+}}{2} (\nabla \cdot \mathbf{u}) &= -\frac{1}{L_{\perp}} \sqrt{\frac{w_{-}}{\rho}} w_{+}, \\ \frac{\partial w_{-}}{\partial t} + \nabla \cdot [(\mathbf{u} - \mathbf{V}_A) w_{-}] + \frac{w_{-}}{2} (\nabla \cdot \mathbf{u}) &= -\frac{1}{L_{\perp}} \sqrt{\frac{w_{+}}{\rho}} w_{-}. \end{aligned}$$

These equations work both for the balanced and moderately imbalanced turbulence and for the balanced turbulence ($w_{+} = w_{-} = w$) they reduce to the equations by *Hollweg* (1986) as described above. For the imbalanced turbulence they properly reduce the dissipation rate for the dominant wave by expressing this rate in terms the amplitude of the minor oppositely propagating wave.

However, the above equations for \mathbf{z}_{\pm} demonstrate that even in a linear approximation the WKB approach dismisses the correlations between inward and outward propagating

waves. Indeed, in the partial differential equation for \mathbf{z}_+ there are the source terms present linearly proportional to \mathbf{z}_- and vice versa, while in the WKB approximation these source terms describing the conversion between the oppositely going waves are omitted. The omitted correlations are important (see *Tu and Marsch (1995); Dmitruk et al. (2002)*) and we will include them into the model as described in the forthcoming publication.

Here, we parameterize this effect in order to incorporate the coronal heating in the coronal holes. The WKB approximation predicts no inward propagating waves originating from the open magnetic field lines, while in reality the inward propagating wave should arise from the partial conversion (“*reflection*”) of the outward propagating wave due to non-WKB effects. *The non-WKB generation of the inward propagating waves is parameterized via their amplitude related to that of the outward propagating waves, so that the maximum of the WKB and non-WKB wave amplitudes is used to determine the dissipation rate of the dominant outward propagating waves:*

$$\frac{\partial w_+}{\partial t} + \nabla \cdot [(\mathbf{u} + \mathbf{V}_A)w_+] + \frac{w_+}{2}(\nabla \cdot \mathbf{u}) = -\frac{1}{L_\perp} \sqrt{\frac{\max(w_-, C_{\text{refl}}^2 w_+)}{\rho}} w_+, \quad (21)$$

$$\frac{\partial w_-}{\partial t} + \nabla \cdot [(\mathbf{u} - \mathbf{V}_A)w_-] + \frac{w_-}{2}(\nabla \cdot \mathbf{u}) = -\frac{1}{L_\perp} \sqrt{\frac{\max(w_+, C_{\text{refl}}^2 w_-)}{\rho}} w_-. \quad (22)$$

2.4.3. Estimates for the Reflection Coefficient

In the present research we focus on the study of the Lower Corona and do not compare the solar wind generation and its propagation towards 1 AU. Therefore, for our present purpose the estimate

$$C_{\text{refl}} = \text{const} \sim 0.01 \div 0.1$$

is sufficient.

Having in mind to develop this approach in the forthcoming publications, we discuss briefly, how the idea of the WSA semi-empirical model can be implemented within the

Alfvén-wave-turbulence-driven model. As discussed above, for the WSA model the speed of the solar wind originating from the given magnetic field line footpoint may be found from two characteristics of the line - the expansion factor, f_{exp} , and the distance to the coronal hole boundary, θ :

$$u_{\infty} = u_{\infty}(\theta, f_{\text{exp}}).$$

In the original version of the WSA model, for example, the solar wind speed, was a function of the expansion factor only: $u_{\infty} = A/f_{\text{exp}}^{\delta}$, where the unknown constants, A and δ were chosen for better fitting the observed solar wind speed at 1 AU.

Once formulated in terms of the Alfvén wave absorption, the model can no longer employ the *existing WSA formulae* for the solar wind, as long as there is no simple relationship between the wave absorption and the solar wind speed. However, we can keep using *the idea of the WSA model* and fit the observed solar wind parameters at 1 AU by properly choosing a formula for C_{refl} that depends on θ and f_{exp} . The first choice to be tested is:

$$C_{\text{refl}} = A \cdot f_{\text{exp}}^{\delta}, \tag{23}$$

where the unknown constants will be chosen to better fit the observations.

Note that there is some reasoning in favor of this approach within the wave-based model for the solar wind, as long as the expansion factor for a given magnetic field line is a good characteristic of the reflection coefficient for the waves, propagating along this line. Indeed, the expansion factor is larger for strongly bent magnetic field lines, but the reflection coefficients at such lines is also larger than on straight lines. At small distances from the coronal boundary the abrupt gradients of the plasma density also can be a reason for the increase in the reflection coefficient (see *Evans et al. (2012)*), resulting in the generally recognized opinion that the slow wind (higher wave absorption) has its origin near the coronal hole boundary (small θ).

3. Computational Model

In this section, we describe the governing equations to be solved numerically as well as the numerical tools we use in the numerical simulations.

3.1. Governing Equations

The model includes the standard MHD equations (non-specified denotations are as usually):

$$\frac{\partial \rho}{\partial t} + \nabla \cdot (\rho \mathbf{u}) = 0, \quad (24)$$

$$\frac{\partial \mathbf{B}}{\partial t} + \nabla \cdot (\mathbf{u} \otimes \mathbf{B} - \mathbf{B} \otimes \mathbf{u}) = 0, \quad (25)$$

$$\frac{\partial (\rho \mathbf{u})}{\partial t} + \nabla \cdot \left(\rho \mathbf{u} \otimes \mathbf{u} - \frac{\mathbf{B} \otimes \mathbf{B}}{\mu_0} \right) + \nabla \cdot \left(P_i + P_e + \frac{B^2}{2\mu_0} + \frac{w_- + w_+}{2} \right) = 0, \quad (26)$$

with the full energy equations applied separately to ions

$$\begin{aligned} \frac{\partial \left(\frac{P_i}{\gamma-1} + \frac{\rho u^2}{2} \right)}{\partial t} + \nabla \cdot \left[\left(\frac{\rho u^2}{2} + \frac{\gamma P_i}{\gamma-1} + \frac{B^2}{\mu_0} \right) \mathbf{u} - \frac{\mathbf{B}(\mathbf{u} \cdot \mathbf{B})}{\mu_0} \right] = \\ = -(\mathbf{u} \cdot \nabla) P_e + \frac{N_i k_B}{\tau_{ei}} (T_e - T_i) + \Gamma_- w_- + \Gamma_+ w_+, \end{aligned} \quad (27)$$

and to electrons:

$$\frac{\partial \left(\frac{P_e}{\gamma-1} \right)}{\partial t} + \nabla \cdot \left(\frac{P_e}{\gamma-1} \mathbf{u} \right) + P_e \nabla \cdot \mathbf{u} = \nabla \cdot (\kappa \nabla T_e) + \frac{N_i k_B}{\tau_{ei}} (T_i - T_e) - Q_{\text{rad}}. \quad (28)$$

In addition to the standard effects, the above equations account for a possible difference in the electron and ion temperatures, the electron heat conduction parallel to the magnetic field lines:

$$\kappa = \frac{\mathbf{B} \otimes \mathbf{B}}{B^2} \kappa_{\parallel}, \quad \kappa_{\parallel} \propto T_e^{5/2} \quad (29)$$

the radiation energy loss from an optically thin plasma:

$$Q_{\text{rad}} = N_e N_i \Lambda(T_e), \quad (30)$$

as well as the energy exchange between electron and ions parameterized via the relaxation time, τ_{ei} , as this is usually done. The Alfvén wave turbulence pressure and dissipation rate is applied in the above equations. In particular simulations, the heating due to the turbulence dissipation (see Eq.27) may be split between electron and ions and we can also use the total energy equation for electron and ions, to improve the computational efficiency. The turbulence propagation and dissipation are described within the WKB approximation:

$$\frac{\partial w_{\pm}}{\partial t} + \nabla \cdot (\mathbf{u}w_{\pm} \pm \mathbf{b}V_A w_{\pm}) + \frac{1}{2}w_{\pm}\nabla \cdot \mathbf{u} = -\Gamma_{\pm}w_{\pm}. \quad (31)$$

The total wave energy dissipation (that is the total of the right hand side of Eqs.(31) taken with the opposite signs), $e = \Gamma_-w_- + \Gamma_+w_+$, is included in the right hand side of the energy equation (27) as the source term. Summarize the above consideration and derivations regarding the dissipation rate (see Eqs.(17,21,22)), which we apply in the following form:

$$\Gamma_{\pm} = \frac{\sqrt{|\mathbf{B}|}}{(L_{\perp} \cdot \sqrt{|\mathbf{B}|})} \sqrt{\frac{\max(w_{\mp}, C_{\text{refl}}^2 w_{\pm})}{\rho}}, \quad (32)$$

and with the following ranges for the parameters involved:

$$(L_{\perp} \cdot \sqrt{|\mathbf{B}|}) = (20 \div 100) \text{ km} \cdot \text{T}^{1/2}, \quad C_{\text{refl}} = 0.01 \div 0.1, \quad (33)$$

We use the simplest equation of state for the coronal plasma with the polytropic index, $\gamma = \frac{5}{3}$.

The system of governing equations is solved numerically using BATS-R-US/SWMF code (see section 3.3 below). The boundary condition for the Poynting flux (or for the intensity of the outgoing waves) is given by Eq.(5) (see Fig. 1). The boundary condition for the coronal magnetic field is taken from the full disk magnetogram. The boundary condition for the density and temperature requires more attention and is discussed in the following subsection.

3.2. Chromosphere and transition region

3.2.1. Chromosphere Boundary Condition

Here, we discuss the analytical solution of the hydrostatic equilibrium and heat transfer equations with the exponential heating function, $Q_h = A \exp(-x/L)$, The solution is as follows:

$$\begin{aligned} T_e = T_i = T_0, \quad N_e = N_i = N_0 \exp\left(-\frac{m_i g x}{k_B(T_e + T_i)}\right), \\ Q_h = Q_{rad} = N_e^2 \Lambda(T_0) = N_0^2 \Lambda(T_0) \exp\left(-\frac{m_i g x}{k_B T_0}\right). \end{aligned} \quad (34)$$

Here $g = 274 \text{ m/s}^2$ is the gravity acceleration near the solar surface, the direction of this acceleration being antiparallel to the x-axis and m_i is the proton mass. The two constants in the solution, N_0 and T_0 , which are the boundary values for the density and temperature correspondingly, are unambiguously related to the amplitude and decay length of the heating function:

$$L = \frac{k_B T_0}{m_i g} \approx T_0 \cdot (30 \text{ m/K}), \quad A = N_0^2 \Lambda(T_0). \quad (35)$$

Notice a very simple relationship for the exponential decay length for the heating function, which is the half of the barometric scale length for density: $2L = L_g = k_B(T_e + T_i)/(m_i g)$.

The described solution satisfies the equation for the heat conduction as long as the heat transfer in the isothermic solution is absent and heating at each point exactly balances the radiation cooling. The hydrostatic equilibrium is also maintained, as long as

$$k_B \frac{\partial(N_e T_e + N_i T_i)}{\partial x} = -g N_i m_i.$$

The suggested solution well describes the chromosphere. The short decay length of the heating function, which is equal to $\approx 0.6 \text{ Mm}$ for $T_0 = 2 \cdot 10^4 \text{ K}$ may be, presumably, related to absorption of (magneto)acoustic turbulent waves, rapidly damping due to the wave-breaking effects, which result in the shock wave formation and energy dissipation. Physically, including this chromosphere heating function would imply that the temperature

in the chromosphere is elevated compared to the photospheric temperatures due to some mechanism acting in the chromosphere itself. By no means can this energy be transported from the solar corona as long as the electron heat conduction rate at chromospheric temperatures is very low.

As long as we do not apply such *ad hoc* short-scale heating function in the chromosphere, nor we include short-scale turbulent dissipation length, *we set the boundary condition for the density and the temperature at the top of chromosphere:*

$$T_{ch} = T_0 = 2 \cdot 10^4 \text{ K}, \quad N_{ch} = N_0 \approx 2 \cdot 10^{16} \text{ m}^{-3} \quad (36)$$

3.2.2. Transition region

The analytical solution for the transition region had been published many times. Here we focus on the following issues: (1) merging this solution to that for the chromosphere; (2) the validity of zero-gravity approximation; and (3) the validity of the modified heat conduction model.

The heat transfer equation for a steady state hydrogen plasma in a uniform magnetic field reads:

$$\frac{\partial}{\partial s} \left(\kappa_0 T_e^{5/2} \frac{\partial T_e}{\partial s} \right) + Q_h - N_e^2 \Lambda(T_e) = 0. \quad (37)$$

Here $Q_h = \Gamma(w_- + w_+)$ is the coronal heating function assumed to be constant at the spatial scales typical for the transition region. Note that the coordinate is taken along the magnetic field line, not along the radial direction.

On multiplying Eq.(37) by $\kappa_0 T_e^{5/2} (\partial T_e / \partial s)$ and by integrating from the interface to chromosphere till a given point at a temperature, T_e , one can obtain:

$$\left[\frac{1}{2} \kappa_0^2 T_e^5 \left(\frac{\partial T_e}{\partial s} \right)^2 + \frac{2}{7} \kappa_0 Q_h T_e^{7/2} \right] \Big|_{T_{ch}}^{T_e} = (N_e T_e)^2 \int_{T_{ch}}^{T_e} \kappa_0 T^{1/2} \Lambda(T) dT. \quad (38)$$

Here the product, $N_e T_e$, is assumed to be constant, therefore, it is separated from the

integrand. For a given T_{ch} the only parameter in the solution is $(N_e T_e)$. It can be expressed at any point in terms of the local value of the heating flux and the radiation loss integral:

$$(N_e T_e) = \sqrt{\frac{\frac{1}{2}\kappa_0^2 T_e^5 \left(\frac{\partial T_e}{\partial s}\right)^2 + \frac{2}{7} \left(\kappa_0 Q_h T_e^{7/2} - \kappa_0 Q_h T_{ch}^{7/2}\right)}{\int_{T_{ch}}^{T_e} \kappa_0 T^{1/2} \Lambda(T) dT}}. \quad (39)$$

The assumption of constant $(N_e T_e)$ is fulfilled only if the effect of gravity is negligible. Quantitatively this condition is not trivial, as long as both the barometric scale and especially the heat conduction scale are the functions of temperature. The barometric scale may be approximated as $L_g(T_e) \approx T_e \cdot (60 \text{ m/K})$. The heat conduction scale, L_h , can be estimated by noticing that within the large part of the transition region the radiation losses dominate over the heating function, therefore, they are balanced by heat conduction: $\kappa_0 T_e^{5/2} \cdot (T_e/L_h^2) \sim Q_r$. Thus, the condition for neglecting gravity is:

$$L_g(T_e) \approx T_e \cdot (60 \text{ m/K}) \gg L_h \approx \sqrt{\frac{\kappa_0 T_e^{9/2}}{\Lambda(T_e)(N_e T_e)^2}}. \quad (40)$$

In Fig. 2 we plot temperature dependencies, $L_h(T_e)$, $L_g(T_e)$, for $(N_e T_e) = 10^{20} \text{ K/m}^3$. We see that near the chromosphere boundary the approximation (40) works very well as long as the temperature changes with height are very abrupt. The increase in temperature till 10^5 K occurs at the length shorter than 0.1 Mm . This estimate agrees with the temperature profile recovered from observations of chromospheric lines (see, e.g., Fig.2 and Fig.8 in *Avrett and Loeser (2008)*). However, as the temperature further grows with the height, the gravity effect on the temperature and density profiles becomes more significant. It becomes comparable with the heat conduction effect at $T_e \approx 4.5 \cdot 10^5 \text{ K}$, which can be accepted as the coronal base temperature, so that the transition region corresponds to the temperature range from $T_{ch} \approx 2 \cdot 10^4 \text{ K}$ till $4.5 \cdot 10^5 \text{ K}$, with a typical width being $\sim 10 \text{ Mm} \approx R_S/70$. The transition region solution merges to the chromosphere solution with negligible jump in pressure. The merging point in the chromosphere, therefore, is at the density of $(N_e T_e)/T_{ch} \sim 10^{16} \text{ m}^{-3}$. The short heat conduction scale at the chromosphere temperature

(see Fig1) ensures that the heat flux from the solar corona across the transition region does not penetrate towards higher densities.

It is known that Eq.(39) may be used to establish the boundary condition for density at the 'coronal base', however, we use another way to model the transition region by increasing artificially the heat conduction in the lower temperature range (see *Abbett* (2007)). Consider a following transformation of the temperature functions in Eqs.(37-38):

$$\kappa_0 \rightarrow f\kappa_0, \quad ds \rightarrow f ds, \quad , \Gamma \rightarrow \Gamma/f, \quad Q_{rad} \rightarrow Q_{rad}/f, \quad (41)$$

with a common factor, $f \geq 1$. The equations does not change in this transformation and the only effect on the solution is that the temperature profile in the transition region becomes a factor of f wider. By applying the factor, $f = (T_m/T_e)^{5/2}$ at $T_{ch} \leq T_e \leq T_m$, one can achieve that the heat conduction scale in this range is almost constant and is close to ≈ 2 Mm for a choice of $T_m \approx 2.2 \cdot 10^5$ K (see Fig. 1).

It should be emphasized, however, that the choice of the temperature range to apply this transformation is highly restricted by the condition as in (40). In choosing a higher value of T_m the heat conduction scale at the chromospheric temperature exceeds the barometric scale in the chromosphere resulting in physically meaningless penetration of the coronal heat to the deeper chromosphere. The global model of the solar corona with this unphysical energy sink suffer from the reduced values of the coronal temperature and produces a visible distortion in the EUV and X-ray synthetic images. *Thus, in formulating the transition region model we modify the heat conduction, the radiation loss rate and the wave dissipation rate and the maximal temperature for this modification does not exceed $T_m \approx 2.2 \cdot 10^5$ K.*

3.3. BATS-R-US and SWMF Codes

The BATS-R-US (Block Adaptive Tree Solar Wind Roe-type Upwind Scheme) code has been developed at the UM. It solves the equations of ideal MHD—a system of eight equations describing the transport of mass, momentum, energy, and magnetic flux (*Groth et al.* 2000; *Powell et al.* 1999). This massively parallel code enables Sun-to-Earth simulations to be performed in near real-time when run on hundreds of processors on a supercomputer (*Manchester et al.* 2004b). The implementation of adaptive-mesh-refinement (AMR) in BATS-R-US allows orders of magnitude variation in numerical resolution within the computational domain. This is important for a global model of the solar magnetic fields in which one strives to resolve such structures as shocks, volumetric currents of flux ropes, electric current sheets in a 3D domain, which may extend out to hundreds of R_{\odot} . The use of AMR also enables us to resolve the fine structure of active regions on the Sun, which spawn CMEs. This is vitally necessary for incorporating high-resolution magnetic data into a numerical MHD model. In the context of solar-heliospheric physics, BATS-R-US has been utilized to model the global structure of the solar corona and solar wind (*Roussev et al.* 2003b; *Cohen et al.* 2007, 2008), as well as the initiation (*Roussev et al.* 2003a; *Jacobs et al.* 2009) and propagation of idealized (*Manchester et al.* 2004a,b) and not-so-idealized (*Roussev et al.* 2004, 2007) solar eruptions and associated SEP events (*Sokolov et al.* 2004).

The SWMF (Space Weather Modeling Framework) is a high-performance computational tool that has been developed at the University of Michigan to simulate the coupled Sun-Earth system (*Tóth et al.* 2004, 2005). One of the main modules within the SWMF is the BATS-R-US MHD code. The SWMF is a structured collection of software building blocks to develop Sun-Earth system modeling components, in order to couple and assemble them into applications. The framework was designed to have “plug-and-play” capabilities, and presently it links together nine inter-operating models of physics domains, ranging

from the surface of the Sun to the upper atmosphere of the Earth. Tying these models together gives a self-consistent whole in which each region is described by a world-class model, and those models communicate data with each other. The SWMF has achieved faster than real-time performance on massively parallel computers, such as the NASA’s Columbia supercluster.

4. Simulation Results for CR2107 and Comparison with Observations

At the rising phase of solar cycle 24, the Sun is becoming more and more active. In this study, we focus on the Carrington Rotation 2107 (From 2011 February 16 to 2011 March 16). During this carrington rotation, a series of interesting events happened on March 7 in NOAA 11164. First, an M3.7 flare occurred around 20:00 UT, followed by a very fast CME with speed $\sim 2200 \text{ km s}^{-1}$. A gradual SEP event was observed at 1 AU, which suggests that the CME-driven shock may play an important role to accelerate particles. Also, gamma-ray emission above 100 MeV was detected by Fermi/LAT and lasted for ~ 8 hr. This is very unusual since the hours-long gamma ray emission from the Sun was observed only three times in the past. Therefore, the flare-related acceleration is extremely strong in this event. By simulating this event and validating the results with the observations, we can achieve a better understanding of the physics behind the varies phenomenon from the Sun to 1 AU.

4.1. Steady State Solar Wind and Validation

To simulate the CR2107, a data-driven boundary condition is used for the inner boundary magnetic field. We use the SDO/HMI synoptic magnetogram in this study (see Fig. 3). Since the uncertainty of the polar region field, a correction is made to the polar field (*Sun et al.* 2011). To extrapolate the initial potential field, Finite Difference

Iterative Potential-field Solver (FDIPS) is used (*Tóth et al.* 2011). The resolution of the magnetogram is 3600×1440 .

A spherical grid is used in the simulation. The simulation domain reaches $20 R_{\odot}$. In total, 1.3×10^5 blocks ($6 \times 4 \times 4$) is used with 1.2×10^7 cells. Adaptive mesh refinement is performed to resolve the heliosphere current sheet (HCS). The smallest cell reaches $\sim 10^{-3} R_{\odot}$, while the largest is $\sim 0.8 R_{\odot}$. The radial velocity at X=0 plane is shown in Fig. 4. The fast and slow winds are evident in that plot. The fast wind is $\sim 600 \text{ km s}^{-1}$. The slow wind is $\sim 300 \text{ km s}^{-1}$.

In Figs. 5-6, zoom-in velocity and plasma beta with magnetic field lines are shown near the Sun. The velocity pattern shows more complex structures comparing with the solar minimum condition. The magnetic field show many structures (e.g., streams, pseudo-streams). From the plot of the plasma beta, we can see the different regions of the corona have very different plasma beta. The polar regions with open field lines have small beta ~ 0.01 near the Sun and increase outward. The high beta regions show the location of the current sheets in which the magnetic field is very small.

In order to evaluate the new steady state solar wind model near the Sun, we compare the model output to the electron temperature and density derived from EUV images of the Sun by using the DENT method (*Vázquez et al.* 2010). In general, the DENT method uses a time series of EUV images under the assumption of no time variation and uniform solar rotation to derive 3D emissivity distribution in each EUV band. By Local Differential Emission Measure (LDEM) analysis, the 3D distribution of the electron density and temperature can be obtained. The DENT method assumes the plasma is optically thin. In this study, we use three bands of EUV observation (171, 193, and 284 Å) from SDO/AIA.

In Figs. 7-8, we show the ratio between the model and DENT output for the electron density and temperature. The sphere is at $r=1.05R_{\odot}$. The ring is between $r=1.035R_{\odot}$ and $r=1.225R_{\odot}$. For the density, we see a good agreement between the model and the DENT

output for most regions. The active regions and polar regions in the model have relatively smaller density (Note that the DENT method has larger uncertainty for the active and polar regions). For temperature, we find the model and DENT have better agreement for higher altitude. The model temperature at $r=1.05R_{\odot}$ is lower than the DENT by a factor of ~ 2 .

In Fig.9 we provide a direct comparison of the observed EUV images with those synthesized from simulations. For better visibility we marked the active regions and coronal holes. One can see that our numerical simulations well reproduce the observed morphological structures, thus confirming the physical reasonings of the new global coronal model.

5. Conclusion and future work

At the present stage the global coronal model which is the heart of the solar-heliosphere model in the SWMF does not employ any longer the *ad hoc* heating function, with no significant loss in the results quality. For the Carrington rotation CR2107 the simulation results are compared with observations. The uncertainty ranges in the model are comparatively narrow, except for the reflection coefficient and the uncertainties may be further reduced in the course of more thorough validation with observations. The contrast ratio in the synthetic images will also be improved.

Another direction for our further investigation is to improve the solar wind model in the way described in sub-subsection 2.4.2. The reflection coefficient at the time is the most uncertain parameter and the only point which is certain about the realistic reflection is that it should account for the wave interaction with realistic gradients of the magnetic field and the coronal density. The solar wind propagation to 1AU and the results comparison with the *in situ* observations will be presented in the accompanying publications.

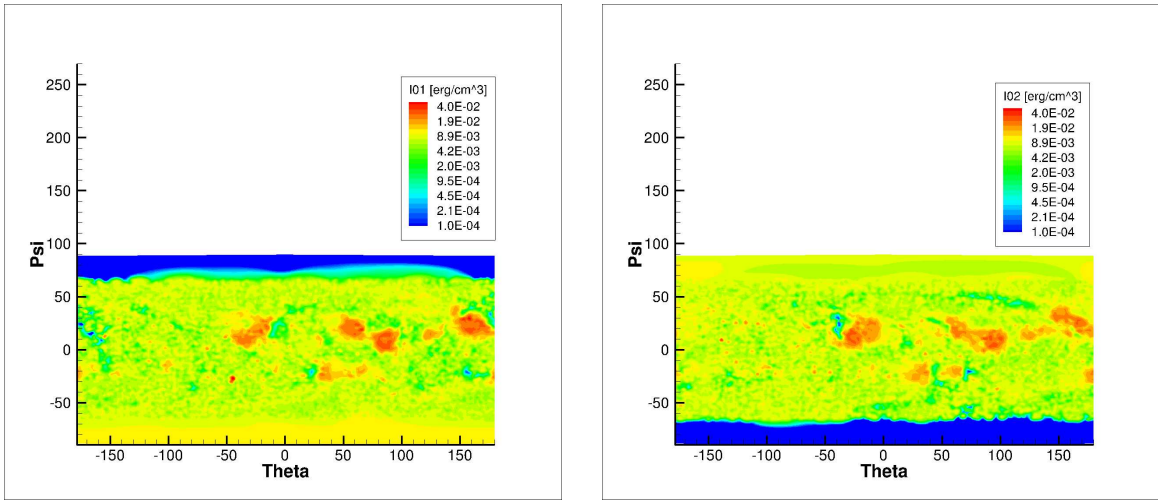


Fig. 1.— The distributions of the wave energy densities, w_+ (left panel), and w_- (right panel), at the heliospheric distance of $1.003 R_\odot$ illustrate boundary conditions for the Poynting flux.

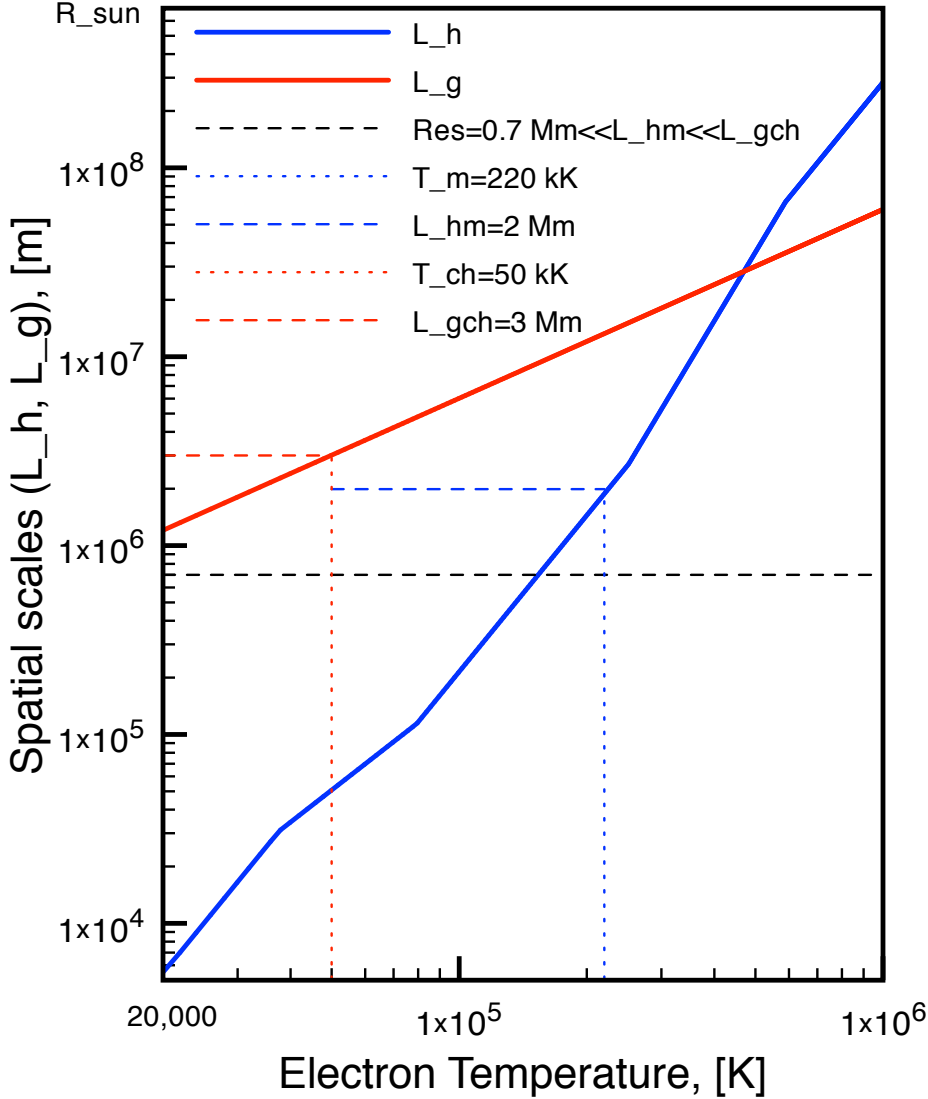


Fig. 2.— Typical scales of the transition region: the heat conduction scale (blue), L_h , and the gravitational height (red), L_g , as functions of the temperature. The real transition region (at $T_e \leq 4 \cdot 10^5$ K) is very narrow comparing to the gravitational height: $L_h \ll L_g$. To keep this property in simulations we chose the chromosphere temperature, $T_{ch} = 5 \cdot 10^4$ K, and the temperature below which to modify the electron heat conduction, $T_m = 2.2 \cdot 10^5$ K, in such a way that $\Delta x < L_h < L_g$ at $T_{ch} \leq T \leq T_m$ with the transition region artificially extended till $L_h(T_m) \approx 2$ Mm. Here $\Delta x = 10^{-3}R_{\odot} = 0.7$ Mm is the spatial resolution of our grid near the Sun.

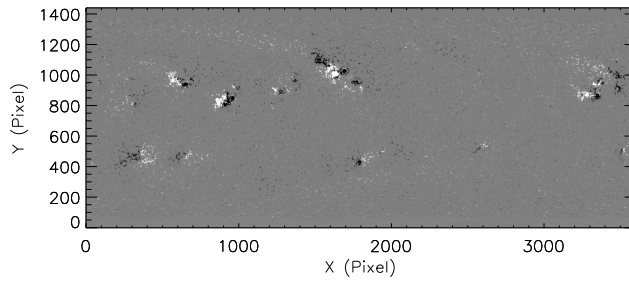


Fig. 3.— The synoptic magnetogram of Carrington Rotation 2107 from SDO/HMI. The saturation value of the magnetic field is set to be 200 Gauss in order to show the active regions more clearly.

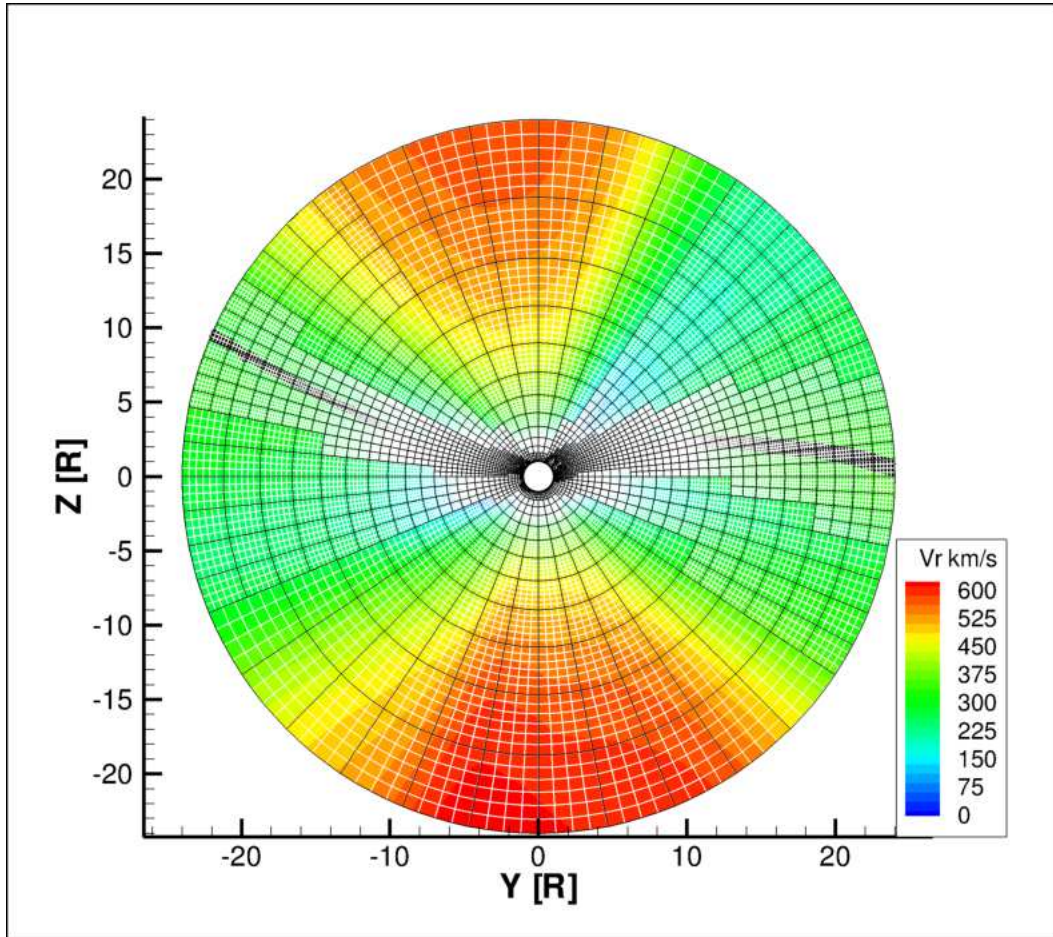


Fig. 4.— The radial velocity of the steady state solar wind at $X=0$ plane. The black boxes in the Figure show the blocks and the white boxes show the cells. The thick black line near the equator shows the location of the heliospheric current sheet.

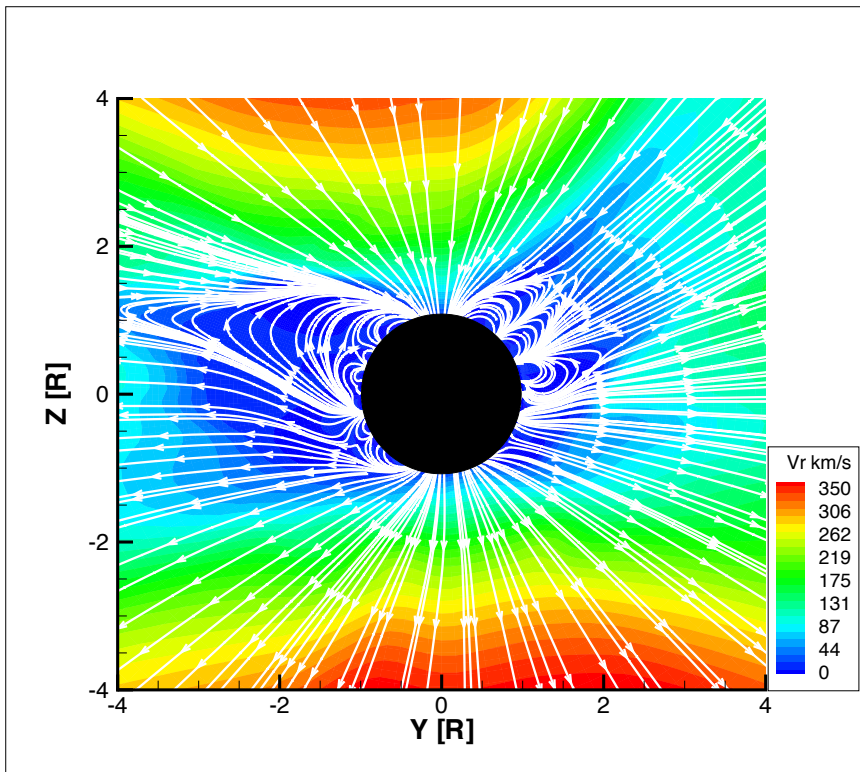


Fig. 5.— The radial velocity field with magnetic field lines at $X=0$ plane from $-4 R_{\odot}$ to $4 R_{\odot}$.

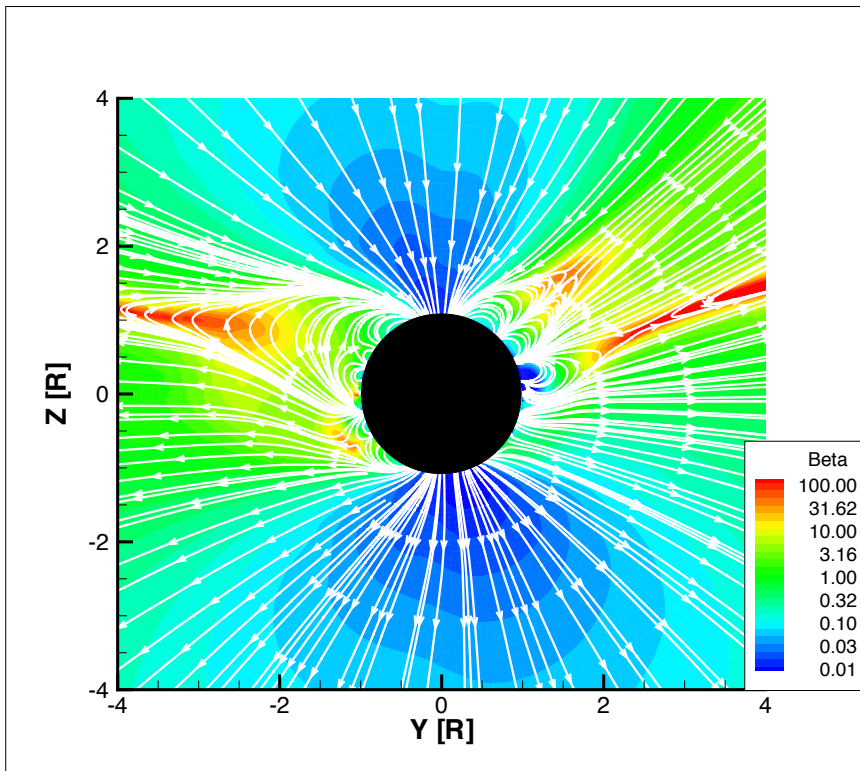


Fig. 6.— The plasma beta with magnetic field lines at $X=0$ plane from $-4 R_{\odot}$ to $4 R_{\odot}$.

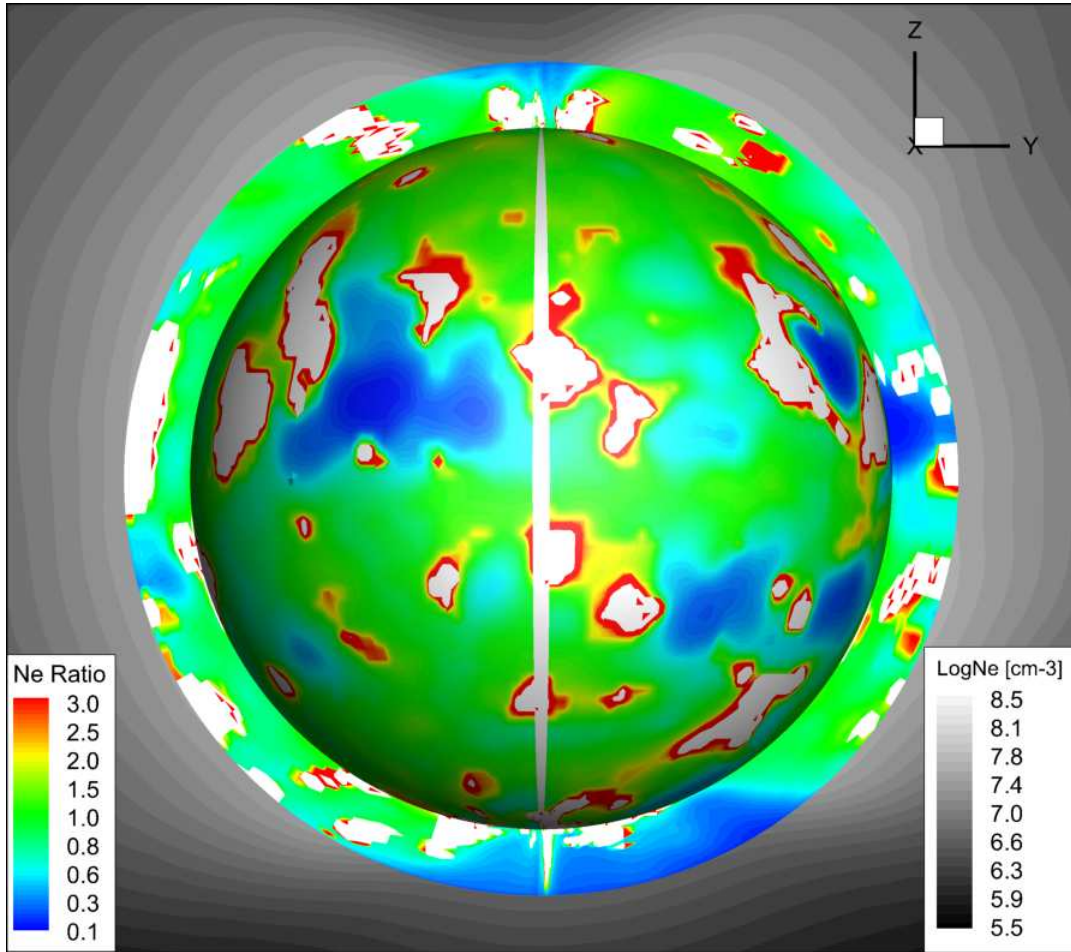


Fig. 7.— Comparison between the SC and DEMT output near the Sun for electron number density. The inner ring shows the ratio between the model and DEMT output from $1.035 R_{\odot}$ to $1.225 R_{\odot}$ and outside background shows the model output. The iso-surface of the Sun shows the same ratio at $R = 1.05 R_{\odot}$.

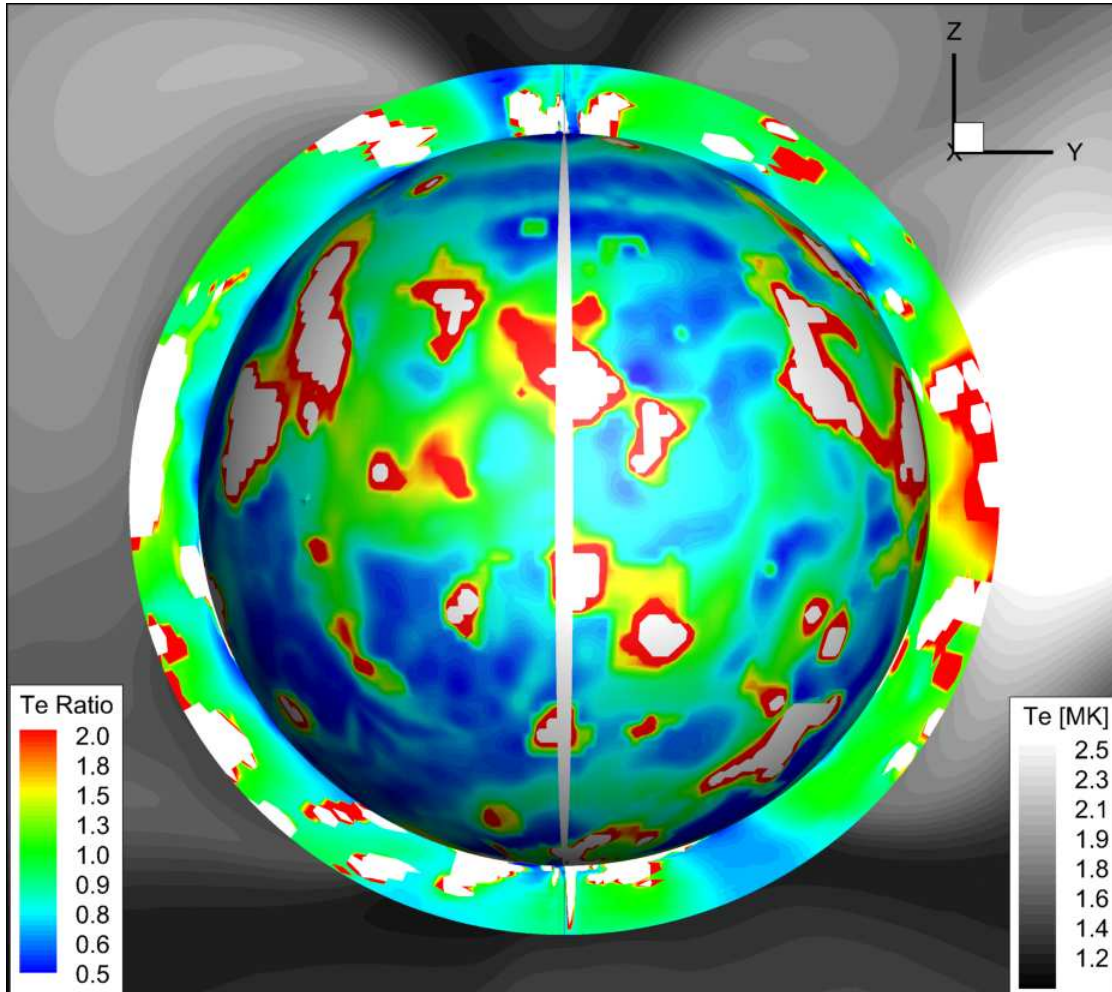


Fig. 8.— Comparison between the SC and DEMT output near the Sun for electron temperature. The inner ring shows the ratio between the model and DEMT output from $1.035 R_{\odot}$ to $1.225 R_{\odot}$ and outside background shows the model output. The iso-surface of the Sun shows the same ratio at $R = 1.05 R_{\odot}$.

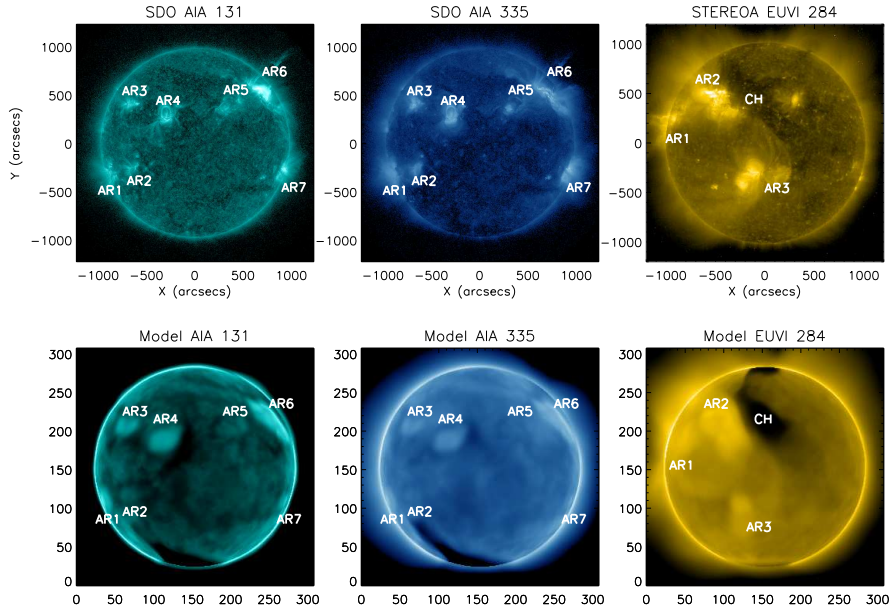


Fig. 9.— The comparison between observations and synthesized EUV images of the model. Top panels (left to right): Observational images from SDO AIA 131 Å, SDO AIA 335 Å, and STEREO A EUVI 284 Å. The observation time is 2011 March 7 20:00 UT. Bottom panels: synthesized EUV images of the model. The active regions and coronal hole are marked both in the observational and synthesized images, to demonstrate the good reproducibility of the observed morphological structures in our simulations.

REFERENCES

- Abbett, W. P., The Magnetic Connection between the Convection Zone and Corona in the Quiet Sun, *Astrophys. J.*, *665*, 1469–1488, August 2007.
- Arge, C. N., and V. J. Pizzo, Improvement in the Prediction of Solar Wind Conditions Using Near-Real Time Solar Magnetic Field Updates, *J. Geophys. Res.*, *105*, 10,465–10,480, May 2000.
- Avrett, E. H., and R. Loeser, C, *Astrophys. J. Suppl.*, *175*, 229, June 2008.
- Cohen, O., I. V. Sokolov, I. I. Roussev, C. N. Arge, W. B. Manchester, T. I. Gombosi, R. A. Frazin, H. Park, M. D. Butala, F. Kamalabadi, and M. Velli, A Semiempirical Magnetohydrodynamical Model of the Solar Wind, *Astrophys. J. Lett.*, *654*, L163–L166, January 2007.
- Cohen, O., I. V. Sokolov, I. I. Roussev, and T. I. Gombosi, Validation of a Synoptic Solar Wind Model, *J. Geophys. Res. (Space Physics)*, *113*(A12), A03104, March 2008.
- Cranmer, S. R., An Efficient Approximation of the Coronal Heating Rate for use in Global Sun-Heliosphere Simulations, *Astrophys. J.*, *710*, 676–688, February 2010.
- De Pontieu, B., S. W. McIntosh, M. Carlsson, V. H. Hansteen, T. D. Tarbell, C. J. Schrijver, A. M. Title, R. A. Shine, S. Tsuneta, Y. Katsukawa, K. Ichimoto, Y. Suematsu, T. Shimizu, and S. Nagata, Chromospheric Alfvénic Waves Strong Enough to Power the Solar Wind, *Science*, *318*, 1574–, December 2007.
- Dmitruk, P., W. H. Matthaeus, L. J. Milano, S. Oughton, G. P. Zank, and D. J. Mullan, Coronal Heating Distribution Due to Low-Frequency, Wave-driven Turbulence, *ApJ*, *575*, 571–577, August 2002.

- Downs, C., I. I. Roussev, B. van der Holst, N. Lugaz, I. V. Sokolov, and T. I. Gombosi, Toward a Realistic Thermodynamic Magnetohydrodynamic Model of the Global Solar Corona, *Astrophys. J.*, 712, 1,219–1,231, April 2010.
- Evans, R. M., M. Opher, R. Oran, B. van der Holst, I. V. Sokolov, R. Frazin, T. I. Gombosi, and A. Vásquez, Coronal Heating by Surface Alfvén Wave Damping: Implementation in a Global Magnetohydrodynamics Model of the Solar Wind, *ApJ*, 756, 155, September 2012.
- Farrugia, C. J., V. A. Osherovich, and L. F. Burlaga, The non-linear evolution of magnetic flux ropes: 3. effects of dissipation, *Annales Geophysicae*, 15, 152–164, February 1997.
- Fisk, L. A., and N. A. Schwadron, The Behavior of the Open Magnetic Field of the Sun, *Astrophys. J.*, 560, 425–438, October 2001.
- Fisk, L. A., N. A. Schwadron, and T. H. Zurbuchen, Acceleration of the Fast Solar Wind by the Emergence of New Magnetic Flux, *J. Geophys. Res.*, 104, 19,765–19,772, September 1999a.
- Fisk, L. A., T. H. Zurbuchen, and N. A. Schwadron, On the Coronal Magnetic Field: Consequences of Large-Scale Motions, *Astrophys. J.*, 521, 868–877, August 1999b.
- Fisk, L. A., Motion of the Footpoints of Heliospheric Magnetic Field Lines at the Sun: Implications for Recurrent Energetic Particle Events at High Heliographic Latitudes, *J. Geophys. Res.*, 101(A7), 15,547–15,554, July 1996.
- Fisk, L. A., On the Global Structure of the Heliospheric Magnetic Field, *J. Geophys. Res. (Space Physics)*, 106(A8), 15,849–15,858, August 2001.
- Groth, C. P. T., D. L. DeZeeuw, T. I. Gombosi, and K. G. Powell, Global Three-Dimensional MHD Simulation of a Space Weather Event: CME Formation,

- Interplanetary Propagation, and Interaction with the Magnetosphere, *J. Geophys. Res.*, *105*, 25,053–25,078, November 2000.
- Hollweg, J. V., Transition Region, Corona and Solar Wind in Coronal Holew, *J. Geophys. Res.*, *91*, 1411–1425, April 1986.
- Hu, Y. Q., R. Esser, and S. R. Habbal, A four-fluid turbulence-driven solar wind model for preferential acceleration and heating of heavy ions, *J. Geophys. Res.*, *105*, 5093–5112, March 2000.
- Jacobs, C., I. I. Roussev, N. Lugaz, and S. Poedts, The Internal Structure of Coronal Mass Ejections: Are all Regular Magnetic Clouds Flux Ropes?, *Astrophys. J. Lett.*, *695*, L171–L175, April 2009.
- Jin, M., B. Manchester, W. B. and van der Holst, J. R. Gruesbeck, R. A. Frazin, E. Landi, A. M. Vasquez, P. L. Lamy, A. Llebaria, A. Fedorov, G. Toth, and T. I. Gombosi, A global two-temperature corona and inner heliosphere model: a comprehensive validation study, *ApJ*, *754*, 6, Mar 2012.
- Li, X., and S. R. Habbal, Coronal Loops Heated by Turbulence-driven Alfvén Waves, *ApJ*, *598*, L125–L128, December 2003.
- Li, G., B. Miao, Q. Hu, and G. Qin, Effect of current sheets on the solar wind magnetic field power spectrum from the ulysses observation: From kraichnan to kolmogorov scaling, *Phys. Rev. Lett.*, *106*, 125001, Mar 2011.
- Lionello, R., J. A. Linker, and Z. Mikić, Including the Transition Region in Models of the Large-Scale Solar Corona, *Astrophys. J.*, *546*, 542–551, January 2001.
- Lionello, R., J. A. Linker, and Z. Mikić, Multispectral Emission of the Sun During the First Whole Sun Month: Magnetohydrodynamic Simulations, *Astrophys. J.*, *690*, 902–912, January 2009.

- Manchester, W. B., T. I. Gombosi, I. Roussev, D. L. De Zeeuw, I. V. Sokolov, K. G. Powell, G. Tóth, and M. Opher, Three-Dimensional MHD Simulation of a Flux Rope Driven CME, *J. Geophys. Res.*, *109(A18)*, 1,102–1,119, January 2004a.
- Manchester, W. B., T. I. Gombosi, I. Roussev, A. Ridley, D. L. De Zeeuw, I. V. Sokolov, K. G. Powell, and G. Tóth, Modeling a Space Weather Event from the Sun to the Earth: CME Generation and Interplanetary Propagation, *J. Geophys. Res.*, *109(A18)*, 2,107–2,122, February 2004b.
- McIntosh, S. W., B. de Pontieu, M. Carlsson, V. Hansteen, P. Boerner, and M. Goossens, Alfvénic waves with sufficient energy to power the quiet solar corona and fast solar wind, *Nature*, *475*, 477–480, July 2011.
- Osman, K. T., W. H. Matthaeus, A. Greco, and S. Servidio, Evidence for Inhomogeneous Heating in the Solar Wind, *Astrophys. J. Lett.*, *727(1)*, January 2011.
- Pevtsov, A. A., G. H. Fisher, L. W. Acton, D. W. Longcope, C. M. Johns-Krull, C. C. Kankelborg, and T. R. Metcalf, The Relationship Between X-Ray Radiance and Magnetic Flux, *Astrophys. J.*, *598*, 1387–1391, December 2003.
- Powell, K. G., P. L. Roe, T. J. Linde, T. I. Gombosi, and D. L. De Zeeuw, A Solution-Adaptive Upwind Scheme for Ideal Magnetohydrodynamics, *J. Comp. Phys.*, *154*, 284–309, September 1999.
- Riley, P., J. A. Linker, Z. Mikić, R. Lionello, S. A. Ledvina, and J. G. Luhmann, A Comparison between Global Solar Magnetohydrodynamic and Potential Field Source Surface Model Results, *Astrophys. J.*, *653*, 1510–1516, December 2006.
- Roussev, I. I., T. G. Forbes, T. I. Gombosi, I. V. Sokolov, D. L. DeZeeuw, and J. Birn, A Three-Dimensional Flux Rope Model for Coronal Mass Ejections Based on a Loss of Equilibrium, *Astrophys. J. Lett.*, *588*, L45–L48, May 2003a.

- Roussev, I. I., T. I. Gombosi, I. V. Sokolov, M. Velli, W. Manchester, D. L. DeZeeuw, P. Liewer, G. Tóth, and J. Luhmann, A Three-Dimensional Model of the Solar Wind Incorporating Solar Magnetogram Observations, *Astrophys. J. Lett.*, 595, L57–L61, September 2003b.
- Roussev, I. I., I. V. Sokolov, T. G. Forbes, T. I. Gombosi, M. A. Lee, and J. I. Sakai, A Numerical Model of a Coronal Mass Ejection: Shock Development with Implications for the Acceleration of GeV Protons, *Astrophys. J. Lett.*, 605, L73–L76, April 2004.
- Roussev, I. I., N. Lugaz, and I. V. Sokolov, New Physical Insight on the Changes in Magnetic Topology during Coronal Mass Ejections: Case Studies for the 2002 April 21 and August 24 Events, *Astrophys. J. Lett.*, 668, L87–L90, October 2007.
- Sokolov, I. V., I. I. Roussev, T. I. Gombosi, M. A. Lee, J. Kóta, T. G. Forbes, W. B. Manchester, and J. I. Sakai, A New Field-Line-Advection Model for Solar Particle Acceleration, *Astrophys. J. Lett.*, 616, L171–L174, December 2004.
- Sokolov, I. V., I. I. Roussev, M. Skender, T. I. Gombosi, and A. V. Usmanov, Transport Equation for MHD Turbulence: Application to Particle Acceleration at Interplanetary Shocks, *Astrophys. J.*, 696, 261–267, May 2009.
- Sun, X., Y. Liu, J. T. Hoeksema, K. Hayashi, and X. Zhao, , *Solar Physics*, 270, 9, September 2011.
- Suzuki, T. K., and S.-i. Inutsuka, Making the Corona and the Fast Solar Wind: A Self-consistent Simulation for the Low-Frequency Alfvén Waves from the Photosphere to 0.3 AU, *Astrophys. J. Lett.*, 632, L49–L52, October 2005.
- Suzuki, T. K., Forecasting Solar Wind Speeds, *Astrophys. J. Lett.*, 640, L75–L78, March 2006.

- Titov, V. S., Z. Mikic, J. A. Linker, and R. Lionello, 1997 May 12 Coronal Mass Ejection Event. I. A Simplified Model of the Preeruptive Magnetic Structure, *Astrophys. J.*, *675*, 1614–1628, March 2008.
- Tóth, G., O. Volberg, A. J. Ridley, T. I. Gombosi, D. L. DeZeeuw, K. C. Hansen, D. Chesney, Q. F. Stout, K. G. Powell, K. Kane, and R. Oehmke, A Physics-Based Software Framework for Sun-Earth Connection Modeling, In Lui, A. T. Y., Y. Kamide, and G. Consolini, editors, *Proc. of the Conf. on the Sun-Earth Connection: Multi-scale Coupling of Sun-Earth Processes*. Elsevier Publ. Co.: Amsterdam, The Netherlands, 2004.
- Tóth, G., I. V. Sokolov, T. I. Gombosi, D. R. Chesney, C. R. Clauer, D. L. De Zeeuw, K. C. Hansen, K. J. Kane, W. B. Manchester, R. C. Oehmke, K. G. Powell, A. J. Ridley, I. I. Roussev, Q. F. Stout, O. Volberg, R. A. Wolf, S. Sazykin, A. Chan, B. Yu, and J. Kóta, Space Weather Modeling Framework: A New Tool for the Space Science Community, *J. Geophys. Res.*, *110*, 12,226–12,237, December 2005.
- Tóth, G., B. van der Holst, and Z. Huang, , *Astrophys. J.*, *732*, 102, September 2011.
- Tu, C.-Y., and E. Marsch, MHD structures, waves and turbulence in the solar wind: Observations and theories, *Space Sci. Rev.*, *73*, 1–210, July 1995.
- Tu, C.-Y., and E. Marsch, Two-Fluid Model for Heating of the Solar Corona and Acceleration of the Solar Wind by High-Frequency Alfvén Waves, *Sol. Phys.*, *171*, 363–391, April 1997.
- Usmanov, A. V., M. L. Goldstein, B. P. Besser, and J. M. Fritzer, A Global MHD Solar Wind Model with WKB Alfvén Waves: Comparison with Ulysses Data, *J. Geophys. Res.*, *105*, 12,675–12,696, June 2000.
- Vásquez, A. M., R. A. Frazin, and W. B. Manchester, , *Astrophys. J.*, *715*, 1352, September 2010.

Verdini, A., M. Velli, W. H. Matthaeus, S. Oughton, and P. Dmitruk, A Turbulence-Driven Model for Heating and Acceleration of the Fast Wind in Coronal Holes, *Astrophys. J. Lett.*, 708, L116–L120, January 2010.